

MedCausalX: Adaptive Causal Reasoning with Self-Reflection for Trustworthy Medical Vision–Language Models

Jianxin Lin^{1,*}, Chunzheng Zhu^{2,*}, Peter J. Kneuert¹, Yunfei Bai³, Yuan Xue^{1,†}
¹The Ohio State University ²Hunan University ³Amazon Web Services

zhuchzh@hnu.edu.cn, Peter.Kneuert@osumc.edu, byunfei@amazon.com, xue.643@osu.edu

Abstract

Vision-Language Models (VLMs) have enabled interpretable medical diagnosis by integrating visual perception with linguistic reasoning. Yet, existing medical chain-of-thought (CoT) models lack explicit mechanisms to represent and enforce causal reasoning, leaving them vulnerable to spurious correlations and limiting their clinical reliability. We pinpoint three core challenges in medical CoT reasoning: how to adaptively trigger causal correction, construct high-quality causal-spurious contrastive samples, and maintain causal consistency across reasoning trajectories. To address these challenges, we propose MedCausalX, an end-to-end framework explicitly models causal reasoning chains in medical VLMs. We first introduce the CRMed dataset providing fine-grained anatomical annotations, structured causal reasoning chains, and counterfactual variants that guide the learning of causal relationships beyond superficial correlations. Building upon CRMed, MedCausalX employs a two-stage adaptive reflection architecture equipped with `<causal>` and `<verify>` tokens, enabling the model to autonomously determine when and how to perform causal analysis and verification. Finally, a trajectory-level causal correction objective optimized through error-attributed reinforcement learning refines the reasoning chain, allowing the model to distinguish genuine causal dependencies from shortcut associations. Extensive experiments on multiple benchmarks show that MedCausalX consistently outperforms state-of-the-art methods, improving diagnostic consistency by +5.4 points, reducing hallucination by over 10 points, and attaining top spatial grounding IoU, thereby setting a new standard for causally grounded medical reasoning.

1. Introduction

Vision-Language Models (VLMs) have shown remarkable potential in medical imaging by coupling visual percep-

* Equal contribution. † Corresponding author.

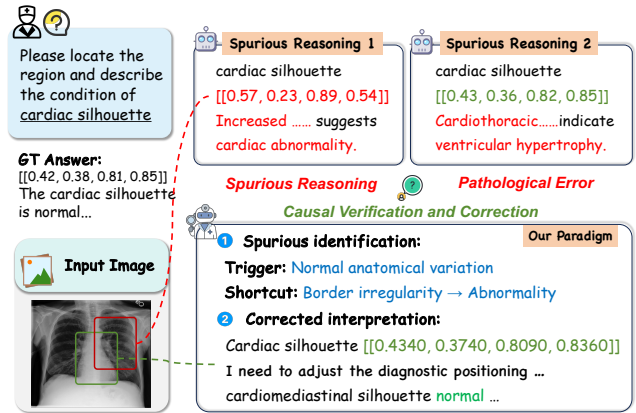


Figure 1. Existing medical VLMs often lack causality-awareness, which manifests as (1) spurious CoT reasoning attends to mislocalized anatomy or (2) overlooking causal evidence for pathology diagnosis. MedCausalX can achieve trustworthy diagnosis by adaptive causal verification and correction during inference.

tion with natural language reasoning for tasks such as diagnostic interpretation and report generation [1, 16, 26]. By processing large-scale multimodal data, these models can provide intelligent clinical decision support [9, 13, 45, 65, 72]. To enhance the reasoning transparency, chain-of-thought (CoT) prompting has been integrated into medical VLMs [35, 49, 59], producing intermediate steps that make the diagnostic process interpretable.

Despite these advances, current medical CoT models lack explicit mechanisms to represent and enforce causal dependencies, which limits their robustness and clinical reliability [19, 41, 47]. As a result, models may implicitly exploit superficial correlations, such as global background features, language model priors, or training distribution biases [84], rather than capturing true causal relations between anatomy, pathology, and diagnosis. This gap between pattern recognition and causal reasoning can lead to explanations that sound plausible yet are not fully aligned with the underlying clinical mechanisms.

In clinical practice, causal reasoning underpins diagnos-

tic reliability [6, 62, 66]. Clinicians reason through a structured chain: identify anatomical abnormalities, interpret pathological manifestations, and draw diagnostic conclusions grounded in established medical knowledge [63, 73]. This process ensures that decisions are supported by causal mechanisms rather than surface correlations, a property current medical VLMs do not yet reliably exhibit.

Despite recent progress in structured reasoning trajectories [35, 59, 68, 95], learning effective dynamic CoT reasoning faces three open challenges. First, how to dynamically identify when causal correction is needed during reasoning rather than statically applying CoT, which can entrench incorrect causal associations. Second, how to construct high-quality contrastive samples that juxtapose causal and non-causal associations to facilitate adaptive reasoning verification while minimizing expert annotation requirements. Third, how to ensure end-to-end causal consistency across the entire reasoning trajectory instead of optimizing token-level likelihoods that ignore global causal coherence.

To systematically address these challenges, we propose MedCausalX, an end-to-end framework that explicitly models causal reasoning with adaptive reflection in medical VLMs. MedCausalX is grounded in three causal insights: (1) Causal compositionality: diagnosis unfolds as a structured causal hierarchy where anatomical localization conditions pathological characterization, and both jointly determine diagnostic conclusions; (2) Causal disruption detection: reasoning failures often arise from local violations of causal dependencies, motivating adaptive reflection to identify and correct these disruptions; and (3) Trajectory-level causal alignment: enforcing global consistency across the reasoning trajectory, beyond token-level likelihood, aligns the model’s reasoning process with causal semantics and discourages reliance on superficial correlations.

Guided by these principles, MedCausalX establishes a unified framework integrating data-level causal supervision, an adaptive reasoning mechanism, and hierarchical optimization into a coherent learning paradigm. It builds upon the CRMed dataset, which provides fine-grained anatomical annotations, structured causal reasoning chains, and counterfactual variants that enable both causal supervision and robustness evaluation. To achieve adaptive reasoning, MedCausalX employs a two-stage reflection mechanism with `<causal>` and `<verify>` tokens to enable autonomous transitions from preliminary causal analysis to verification and correction. Finally, a hierarchical causal optimization pipeline sequentially integrates trajectory-level supervised learning with reinforcement learning on error-attributed trajectories, enforcing causal consistency across the reasoning process and disentangling genuine causal dependencies from shortcut associations.

Extensive evaluation across multiple medical imaging benchmarks demonstrates that MedCausalX substantially

improves compositional reasoning capabilities, enhancing diagnostic consistency, spatial localization, and hallucination suppression while consistently surpassing state-of-the-art methods. These results signify a paradigm shift from correlation-driven pattern matching toward causally grounded and trustworthy multimodal medical AI. The main contributions of this paper are as follows:

- We build CRMed, a dataset containing fine-grained causal reasoning chains and counterfactual variants, designed to support causal supervision in medical vision-language models.
- We introduce a reflection-driven causal reasoning paradigm that enables models to *detect and correct causal disruptions* during inference, transforming static chain-of-thought reasoning into an adaptive process.
- We design a unified learning framework that *aligns reasoning trajectories with causal semantics*, integrating trajectory-level supervision with error-attributed reinforcement learning to suppress shortcut associations.
- MedCausalX achieves consistent gains across diverse medical benchmarks, substantially improving localization accuracy, diagnostic consistency, and interpretability, marking a step toward clinically reliable multimodal AI.

2. Related Works

Chain-of-Thought and Self-Reflection. Chain-of-thought (CoT) enhances reasoning by decomposing complex problems into intermediate steps [33, 43, 75, 79]. Some methods further improve CoT through diverse path sampling and majority voting [76] and demonstrates that CoT can emerge without explicit prompting via alternative decoding strategies [75]. However, these methods struggle with autonomous self-correction without external feedback [8, 25], occasionally degrading after intrinsic correction attempts. Training-based approaches show promise via reinforcement learning [34] and reflection mechanisms [55, 57, 69]. In medical contexts, reflection-based methods enable physician-like reasoning via hypothesis validation [26]. Recent works have further improved VLM reasoning via structured knowledge integration and spatial understanding [23, 54, 80, 81, 85]. However, current approaches lack mechanisms to dynamically determine when causal reasoning should be invoked. Our reflection-token mechanism enables adaptive reasoning selection and explicit verification of causal decomposition.

Causal Reasoning in Medical Imaging. Causal reasoning addresses fundamental limitations of correlation-based learning that remains vulnerable to spurious associations and dataset shift [6, 19, 47, 97]. VLMs have been widely applied across various domains [14, 15, 18, 70, 78, 83, 90, 99], and in the medical field, VLMs have advanced diagnostic reasoning by jointly processing visual and textual in-

formation [24, 28, 29, 39, 51, 52, 59], with chain-of-thought prompting showing promise in multi-step clinical reasoning [35, 49]. Existing studies mitigate confounding through statistical interventions [86] or counterfactual modeling [4], yet these methods are limited to specific question-answering setups. Our framework introduces structured causal annotations and controlled interventions that enable systematic modeling from anatomical localization through pathological characterization to diagnostic inference.

Reinforcement Learning Optimization. Reinforcement learning aligns large language models through iterative policy refinement [3, 42, 58, 71, 92, 93, 100, 101]. Reinforcement Learning from Human Feedback (RLHF) establishes the foundational paradigm with supervised fine-tuning, reward modeling, and policy optimization [12, 67, 77, 88, 89, 102]. Efficient alternatives include Direct Preference Optimization (DPO) [64], and Group Relative Policy Optimization (GRPO), which improves efficiency through group-level advantage estimation [20, 23, 68]. Recent analyses have revealed theoretical limitations of group-based methods, including biased advantage estimation [31, 61, 87], sparse process-level guidance [17], and sensitivity to divergence choices [38]. In medical reasoning, composite reward functions incorporating diagnostic accuracy, causal consistency, and format validity have shown promise [7, 35, 40, 59], with contrast-driven approaches further improving reward reliability [46]. Existing systems often apply uniform corrections [50], whereas our error-attributed policy optimization effectively localizes causal failures and builds targeted preference pairs for fine-grained refinement.

3. Methodology

3.1. Inductive Causal Reasoning via CRMed

We aim to address two critical limitations of current MedCoT approaches: first, reasoning annotations are often post-hoc rationalizations generated by LLMs rather than faithful reflections of clinical reasoning, which may introduce systematic biases and reinforce spurious associations; second, existing datasets typically lack fine-grained anatomical grounding, limiting their ability to support causal analysis in medical imaging contexts.

Structured causal factorization. We model diagnostic reasoning as a structured conditional generation process over three semantically grounded variables: anatomical annotation A , pathological characterization P , and diagnostic conclusion Y . Conditioned on medical image I and clinical query q , we factorize the *joint conditional distribution* as

$$p_{\theta}(Y, P, A | I, q) = p_{\theta}(Y | A, P, I, q) \cdot p_{\theta}(P | A, I, q) \cdot p_{\theta}(A | I, q). \quad (1)$$

This factorization reflects a clinically motivated reasoning order from anatomical grounding to pathological interpretation and finally diagnostic decision.

Structural causal model. We formulate diagnostic reasoning under a structural causal model (SCM):

$$\mathcal{M} = \langle \mathcal{V}, \mathcal{U}, \mathcal{F}, P(\mathcal{U}) \rangle, \quad (2)$$

where $\mathcal{V} = \{A, P, Y\}$, $\mathcal{U} = \{X_v, X_t, U_c\}$ denotes the exogenous variables in the SCM, where X_v and X_t denote latent variability in the visual and textual domains respectively, while U_c represents unobservable confounders that persist throughout the reasoning chain.

The deterministic structural functions $\mathcal{F} = \{\Phi_L, \Phi_P, \Phi_D\}$ define the generative mechanisms as follows:

$$\begin{aligned} A &= \Phi_L(I, q, X_v, U_c), \\ P &= \Phi_P(A, X_v, X_t, U_c), \\ Y &= \Phi_D(P, X_v, X_t, U_c). \end{aligned} \quad (3)$$

We assume the exogenous variables are mutually independent, i.e., $P(\mathcal{U}) = P(X_v)P(X_t)P(U_c)$. This SCM induces a directed acyclic graph (DAG) where the primary clinical flow $A \rightarrow P \rightarrow Y$ is subject to spurious correlations induced by the confounders.

Approximate interventions via localized perturbations.

To distinguish genuine causal reasoning from shortcut correlations, CRMed constructs intervention-inspired samples through *localized perturbations* that selectively alter anatomical or pathological factors while keeping unrelated evidence as stable as possible. For anatomy-targeted perturbations, we modify spatial grounding signals, e.g., replacing bounding box annotations or synthesizing counterfactual variants with altered anatomical structures. For pathology-targeted perturbations, we modify pathological attributes within a fixed anatomical region, e.g., by replacing pathology labels under the same localization or rewriting the pathological component in the reasoning chain. We denote the resulting perturbed input as I^{int} .

These perturbations are intended as *proxy interventions* that approximate manipulations of the corresponding semantic variables (anatomical or pathological) under a locality assumption, rather than exact Pearlian interventions on the endogenous variables. Accordingly, they should be interpreted as practical approximations to $do(A=\tilde{a})$ or $do(P=\tilde{p})$, rather than exact structural interventions that replace the underlying structural equations.

Interventional sample sets. To separate robust causal reasoning from spurious pattern matching, CRMed incorporates three types of samples:

$$\mathcal{D}_{\text{shortcut}} = \{(I^{\text{int}}, q, \tilde{a}, p, C^{\text{spur}}, y)\}, \quad (4)$$

$$\mathcal{D}_{\text{partial}} = \{(I^{\text{int}}, q, a, \tilde{p}, C^{\text{flaw}}, y)\}, \quad (5)$$

$$\mathcal{D}_{\text{causal}} = \{(I, q, a, p, C^{\checkmark}, y)\}, \quad (6)$$

where \tilde{a} and \tilde{p} denote perturbed anatomical and pathological factors, respectively, C^{spur} indicates shortcut-prone reasoning chains, C^{flaw} denotes logically inconsistent pathological

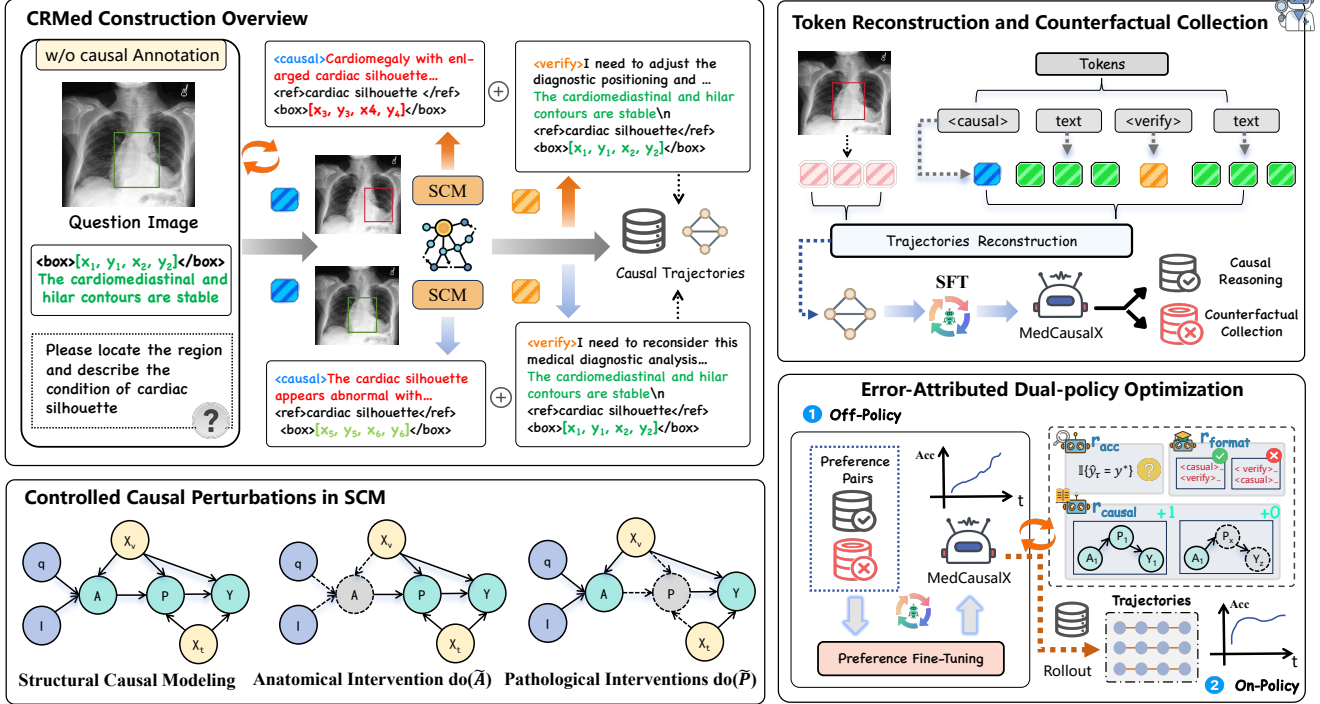


Figure 2. Overview of MedCausalX framework. We first construct CRMed dataset via fine-grained annotations, then factorize reasoning via a structural causal model (SCM) with reflective tokens (`<causal>`, `<verify>`) enabling two-stage adaptive reasoning. After causal Supervised Fine-Tuning (SFT), MedCausalX is subsequently optimized via dual-policy that couples off-policy preference alignment (DPO) with on-policy causal reinforcement (GRPO), bridging stability and adaptability to enhance the model’s causal reasoning capability.

analysis, and C^\checkmark represents clinically grounded causal reasoning chains.

Reflective token augmentation for unified reasoning. Clinical diagnosis relies on iterative self-examination: practitioners continuously revisit and revise hypotheses upon recognizing potential errors, rather than proceeding linearly from observation to conclusion [98]. To instantiate this reflective process, we augment the base vocabulary \mathcal{V}_0 with reflective tokens $\mathcal{T} = \{\langle \text{CAUSAL} \rangle, \langle \text{VERIFY} \rangle\}$, enabling dynamic transitions between preliminary causal analysis and verification-based correction.

During training, all samples in CRMed follow a unified sequence structure:

$$\mathcal{S} = (I, q, \langle \text{CAUSAL} \rangle, R^{\text{biased}}, \langle \text{VERIFY} \rangle, R^{\text{gold}}, y), \quad (7)$$

where $R^{\text{biased}} \in \{C^{\text{spur}}, C^{\text{flaw}}\}$ represents reasoning chains containing spurious correlations or logical inconsistencies from $\mathcal{D}_{\text{shortcut}}$ or $\mathcal{D}_{\text{partial}}$, and $R^{\text{gold}} = C^\checkmark$ denotes clinically validated ground-truth causal chains from $\mathcal{D}_{\text{causal}}$. This construction enforces a two-stage reasoning protocol: the model first generates a preliminary causal analysis conditioned on `<CAUSAL>`, then performs verification and correction triggered by `<VERIFY>`, ultimately producing refined reasoning chains with enhanced causal consistency. This

format enables the model to learn adaptive causal correction through contrastive exposure to both erroneous and correct reasoning trajectories within a unified training paradigm.

3.2. Causal Reasoning Optimization

We adopt a two-stage optimization that explicitly attributes causal errors and strengthens reasoning robustness:

3.2.1. Preliminary: SFT with Causal Decomposition

In this stage, we establish foundational causal reasoning and self-correction capabilities through supervised fine-tuning on the CRMed dataset, maximizing the joint likelihood of generating anatomical localization, causal reasoning chains, and diagnostic predictions, conditioned on the medical image-query pair.

$$\mathcal{L}_{\text{SFT}}(\theta) = -\mathbb{E}_{(I, q, L, C, y) \sim \mathcal{D}} [\log p_\theta(L, C, y | I, q, \mathcal{T})], \quad (8)$$

where \mathcal{T} denotes the reflective token conditioning the reasoning mode, L represents the anatomical localization, C the causal chain, and y the final diagnostic label.

3.2.2. Refinement: Error-Attributed Optimization

After supervised trajectory fine-tuning (Eq. 8), we further refine causal reasoning via reinforcement learning. The training is divided into two complementary stages: an

off-policy preference optimization stage for efficient error correction and an on-policy reinforcement learning stage for adaptive causal refinement. Details of both training paradigms are provided below.

Stage I: Off-policy Training. We leverage collected error trajectories $\mathcal{D}_{\text{error}} = \{(x_{I\&T}^i, Y_{\text{err}}^i, Y_{\text{corr}}^i)\}_{i=1}^{N_e}$ to construct preference pairs for Direct Preference Optimization (DPO). For each input $x_{I\&T}$, we enforce $Y_{\text{corr}} \succ Y_{\text{err}}$ and optimize:

$$\mathcal{L}_{\text{DPO}}(\pi_\theta; \pi_{\text{ref}}) = -\mathbb{E}_{(x, Y_w, Y_l) \sim \mathcal{D}_{\text{error}}} \left[\log \sigma \left(\beta \log \frac{\pi_\theta(Y_w|x)}{\pi_{\text{ref}}(Y_w|x)} \right) - \beta \log \frac{\pi_\theta(Y_l|x)}{\pi_{\text{ref}}(Y_l|x)} \right], \quad (9)$$

where $Y_w = Y_{\text{corr}}$ denotes winning trajectory, $Y_l = Y_{\text{err}}$, π_θ is the trainable policy, π_{ref} the reference policy, $\beta > 0$ the KL coefficient, and $\sigma(\cdot)$ the sigmoid function.

Error Localization Mechanism. To enhance preference pair informativeness, we precisely identify the failure point t_{fail} via step-wise semantic divergence detection:

$$t_{\text{fail}} = \min \{t \in \{1, 2\} : \mathcal{S}(Y_{\text{err}}^t, Y_{\text{gt}}^t) < \tau\}, \quad (10)$$

where $\mathcal{S}(\cdot, \cdot) : \mathcal{Y} \times \mathcal{Y} \rightarrow [0, 1]$ measures semantic similarity and $\tau \in (0, 1)$ is a divergence threshold. We then contrast the continuations $Y_{\geq t_{\text{fail}}}^{\text{err}}$ and $Y_{\geq t_{\text{fail}}}^{\text{corr}}$ while conditioning on the shared prefix $Y_{< t_{\text{fail}}}^{\text{corr}}$, concentrating learning on critical divergence points and improving sample efficiency.

Stage II: On-policy Training. Building on error-localized and high-quality samples, we adopt Group Relative Policy Optimization (GRPO) for on-policy refinement. For each input (x, y^*) , we sample G trajectories $\{\tau_g\}_{g=1}^G$ from π_θ and compute a composite reward $R^{(g)} = R_{\text{total}}(\tau_g, y^*)$ measuring correctness and reasoning quality:

$$\mathcal{L}_{\text{GRPO}} = -\mathbb{E}_{\{\tau_g\}_{g=1}^G \sim \pi_\theta} \left[\frac{1}{G} \sum_{g=1}^G A^{(g)} \log \pi_\theta(\tau_g | x) \right], \quad (11)$$

with group-relative advantage $A^{(g)} = (R^{(g)} - \bar{R}) / (\sigma_R + \epsilon)$, where \bar{R} and σ_R are the mean and standard deviation of rewards within the group. This intra-group normalization stabilizes updates and reduces variance, improving efficiency.

Composite Reward Function. The overall reward is formulated as $R(\tau) = R_{\text{acc}}(\tau, y^*) + R_{\text{format}}(\tau) + R_{\text{causal}}(\tau)$, integrating three complementary components that jointly evaluate reasoning quality from predictive accuracy, structural validity, and causal coherence.

(1) *Accuracy Reward:* $R_{\text{acc}}(\tau, y^*) = \mathbb{I}\{\hat{y}_\tau = y^*\}$, where \hat{y}_τ and y^* denote the model’s output and the correct label, respectively. This term assesses whether the final prediction matches the ground truth.

(2) *Format Reward* is used to ensure structural integrity:

$$R_{\text{format}}(\tau) = \frac{1}{|\tau|} \sum_{t=1}^{|\tau|} \mathbb{I}\{w_t \in \mathcal{V}_{\text{valid}}\}, \quad (12)$$

where $|\tau|$ is the trajectory length, w_t the t -th token, and $\mathcal{V}_{\text{valid}}$ the predefined valid token set. We assess whether correction or verification tokens follow the desired format.

(3) *Causal Consistency Reward* evaluates the logical coherence across consecutive reasoning steps:

$$R_{\text{causal}}(\tau) = \frac{1}{|\mathcal{S}_\tau| - 1} \sum_{i=1}^{|\mathcal{S}_\tau| - 1} \text{Cons}(s_i, s_{i+1}), \quad (13)$$

where $\mathcal{S}_\tau = \{s_1, \dots, s_{|\mathcal{S}_\tau|}\}$ represents the reasoning sequence extracted from trajectory τ , and $\text{Cons}(s_i, s_{i+1})$ quantifies the causal consistency between consecutive steps.

Together, these rewards encourage predictions that are accurate, structurally well-formed, and causally coherent, ensuring that model refinements not only correct errors but also preserve the integrity of underlying causal reasoning.

4. Experiments

4.1. Experimental Setup

Baselines. We compare our method with three comprehensive categories of baselines: (1) General Vision-Language Models, including InternVL [10], GPT-4V [27], and Qwen2.5-VL [2], which exhibit strong multimodal understanding capabilities; (2) Medical-Specific VLMs, such as Med-Flamingo [56], LLaVA-Med [37], RadFM [82], MedDr [21], BiomedGPT [94], and MedRegA [74], representing the state-of-the-art in medical vision-language understanding; and (3) Medical Chain-of-Thought Models, including MedVLM-R1 [59] and Med-R1 [35], which incorporate CoT reasoning processes for interpretability.

Comparison Benchmarks. We evaluate MedCausalX across five medical imaging benchmarks. *MIMIC-CXR* [32] contains chest X-ray image-report pairs for report generation. *SLAKE* [44] and *VQA-RAD* [36] provide multimodality radiology images with clinical question-answer pairs for visual question answering. *PathVQA* [22] focuses on histopathological image reasoning. *SA-Med2D-20M* [91] supports two region-centric tasks with pixel-level annotations: Region-to-Text Identification requires recognizing anatomical structures given bounding boxes, while Text-to-Region Detection requires localizing specific organs or anomalies from textual descriptions. All experiments use 5-fold cross-validation for statistical reliability.

Implementation Details and Evaluation Metrics. MedCausalX builds upon Qwen2.5-VL architecture [5] with model variants ranging from 3B to 32B parameters. Our

Table 1. Comprehensive quantitative comparison on diverse region-centric tasks, including region-to-text identification and text-to-region detection. Abbreviations in this Table: Obj-F1 denotes Object F1, Reg-F1 denotes Region F1, Align-F1 denotes Alignment F1, and Acc denotes Accuracy. The best results are highlighted in **bold**, while the second-best are underlined.

Method	Region-to-Text Identification										Text-to-Region Detection							
	Structure Identification					Lesion Identification					Single-Region Detection				Multi-Region Detection			
	BLEU-1	F1	Recall	BertScore	Acc	BLEU-1	F1	Recall	BertScore	Acc	Obj-F1	Reg-F1	Align-F1	IoU	Obj-F1	Reg-F1	Align-F1	IoU
Qwen2.5-VL [2]	0.15	0.25	0.58	52.34	0.12	0.14	0.23	0.55	48.56	0.11	57.82	8.15	6.23	17.45	49.35	5.87	4.65	14.82
InternVL [11]	0.13	0.21	0.52	51.78	0.11	0.13	0.20	0.51	47.92	0.10	56.60	7.24	5.45	16.61	48.23	5.41	4.18	13.99
Med-Flamingo [56]	0.13	0.72	4.90	24.87	0.01	0.12	0.68	4.72	23.45	0.01	18.47	2.35	1.82	5.23	12.68	1.54	1.18	3.47
LLaVA-Med [37]	0.43	1.15	10.69	34.53	1.74	0.38	1.05	9.85	32.18	1.52	24.83	3.76	2.94	7.85	18.95	2.42	1.87	5.36
RadFM [82]	0.35	0.80	4.75	37.07	1.88	0.32	0.75	4.42	35.62	1.68	21.56	3.12	2.38	6.74	15.82	1.98	1.52	4.58
MedDr [21]	0.75	1.27	3.52	50.28	1.36	0.68	1.18	3.28	48.56	1.24	28.34	4.25	3.47	9.16	22.47	2.85	2.24	6.42
MedRegA [74]	<u>78.34</u>	<u>78.95</u>	<u>79.02</u>	91.63	<u>73.06</u>	<u>61.09</u>	<u>61.90</u>	<u>63.07</u>	82.62	<u>59.42</u>	<u>77.93</u>	<u>45.11</u>	<u>36.53</u>	<u>42.70</u>	<u>68.52</u>	<u>24.78</u>	<u>22.36</u>	<u>31.63</u>
MedCausalX	80.11	80.47	81.63	<u>88.72</u>	<u>75.52</u>	63.65	64.78	66.02	<u>82.10</u>	61.72	82.83	47.05	45.12	44.68	72.75	29.83	27.01	36.02

Table 2. Performance comparison on medical VQA benchmarks with causal reasoning evaluation. Metrics include answer Accuracy (Acc), Diagnostic Consistency (Diag-C), and Hallucination Rate (Hall, lower is better). Results are reported as mean_{std} over 5-fold cross-validation. Best results in **bold**, second-best underlined. '*' denotes fine-tuned models.

Method	SLAKE [44]			VQA-RAD [36]			PathVQA [22]			PMC-VQA [96]			Average		
	Acc	Diag-C	Hall↓												
General Vision-Language Models															
Qwen2.5-VL [2]	68.5 _{1.8}	58.3 _{2.1}	62.5 _{1.9}	52.4 _{2.3}	54.2 _{2.0}	65.8 _{1.7}	48.3 _{2.1}	52.8 _{1.9}	68.2 _{2.2}	58.2 _{1.6}	56.7 _{1.8}	63.5 _{2.0}	56.9 _{1.9}	55.5 _{1.9}	65.0 _{1.9}
InternVL [11]	70.8 _{1.6}	61.2 _{1.8}	59.8 _{2.1}	55.1 _{2.0}	57.5 _{1.9}	62.5 _{1.8}	52.7 _{1.9}	55.3 _{2.0}	65.3 _{2.1}	61.5 _{1.5}	59.2 _{1.7}	60.8 _{1.9}	60.0 _{1.8}	58.3 _{1.9}	62.1 _{2.0}
Medical-Specific Vision-Language Models															
Med-Flamingo [56]	33.2 _{2.7}	38.5 _{2.5}	75.2 _{2.3}	44.6 _{2.6}	42.8 _{2.4}	71.8 _{2.5}	47.9 _{2.4}	45.6 _{2.3}	68.5 _{2.6}	35.9 _{2.8}	40.5 _{2.5}	73.8 _{2.4}	40.4 _{2.6}	41.9 _{2.4}	72.3 _{2.5}
LLaVA-Med [37]	45.6 _{2.3}	46.8 _{2.2}	68.5 _{2.4}	27.4 _{2.8}	40.2 _{2.5}	74.5 _{2.3}	58.2 _{2.0}	53.2 _{2.1}	63.8 _{2.2}	63.8 _{1.8}	55.5 _{2.0}	65.2 _{2.1}	48.8 _{2.2}	48.9 _{2.2}	68.0 _{2.3}
RadFM [82]	82.3 _{1.2}	70.8 _{1.4}	51.2 _{1.8}	60.6 _{1.7}	63.5 _{1.5}	55.8 _{1.9}	40.2 _{2.4}	50.8 _{2.1}	66.5 _{1.8}	45.8 _{2.2}	56.2 _{1.9}	62.8 _{1.7}	57.2 _{1.9}	60.3 _{1.7}	59.1 _{1.8}
MedDr [21]	83.4 _{1.1}	72.5 _{1.3}	48.5 _{1.7}	<u>78.5</u> _{1.3}	70.2 _{1.4}	50.2 _{1.8}	62.8 _{1.6}	64.8 _{1.5}	56.8 _{1.9}	66.2 _{1.5}	66.5 _{1.4}	54.5 _{1.8}	72.7 _{1.4}	68.5 _{1.4}	52.5 _{1.8}
MedRegA [74]	84.1 _{1.0}	<u>73.8</u> _{1.2}	<u>47.8</u> _{1.6}	76.9 _{1.2}	<u>69.5</u> _{1.3}	<u>50.8</u> _{1.7}	<u>68.5</u> _{1.4}	<u>68.5</u> _{1.3}	<u>52.5</u> _{1.8}	<u>79.5</u> _{1.1}	<u>72.8</u> _{1.2}	<u>49.8</u> _{1.6}	<u>77.3</u> _{1.2}	<u>71.2</u> _{1.3}	<u>50.2</u> _{1.7}
Medical Chain-of-Thought Models															
MedCoT [49]*	83.9 _{1.1}	71.5 _{1.3}	49.5 _{1.7}	75.8 _{1.3}	68.2 _{1.4}	52.2 _{1.8}	66.2 _{1.5}	66.8 _{1.4}	54.8 _{1.9}	80.3 _{1.0}	71.8 _{1.2}	50.5 _{1.7}	76.6 _{1.2}	69.6 _{1.3}	51.8 _{1.8}
MedVLM-R1 [59]*	85.7 _{0.9}	75.5 _{1.1}	45.2 _{1.5}	77.3 _{1.2}	71.8 _{1.2}	47.5 _{1.6}	70.8 _{1.3}	70.5 _{1.2}	49.8 _{1.7}	82.4 _{0.9}	75.2 _{1.1}	45.8 _{1.5}	79.1 _{1.1}	73.3 _{1.2}	47.1 _{1.6}
Med-R1 [35]*	85.4 _{0.9}	74.8 _{1.1}	46.5 _{1.6}	76.9 _{1.2}	70.5 _{1.3}	48.8 _{1.7}	69.5 _{1.4}	69.2 _{1.3}	51.5 _{1.8}	81.9 _{1.0}	74.5 _{1.1}	47.2 _{1.6}	78.4 _{1.1}	72.3 _{1.2}	48.5 _{1.7}
MedCausalX (Ours)	87.2 _{0.8}	81.5 _{1.0}	34.2 _{1.4}	79.8 _{1.1}	77.3 _{1.1}	36.5 _{1.5}	73.2 _{1.2}	75.8 _{1.1}	38.9 _{1.6}	84.6 _{0.8}	80.2 _{1.0}	35.8 _{1.4}	81.2 _{1.0}	78.7 _{1.1}	36.4 _{1.5}

main experiments utilize the 32B variant for optimal causal reasoning capabilities. Training follows a two-stage paradigm: Stage I performs supervised fine-tuning on CRMed utilizing causal decomposition objectives (Eq. 8) for 3 epochs; Stage II applies preference optimization, combining off-policy DPO (2 epochs) with on-policy GRPO (2000 steps) to enhance causal consistency. Error localization employs semantic similarity threshold $\tau = 0.7$ for failure point identification. We use AdamW optimizer [30, 53, 60] ($lr = 1 \times 10^{-6}$) and train on 6 NVIDIA A100 GPUs with mixed precision. The causal consistency function $\text{Cons}(s_i, s_{i+1})$ is implemented via an LLM-as-judge protocol: we prompt GPT-4o to assess whether consecutive reasoning steps maintain valid causal dependencies and whether the corrective action triggered by $\langle \text{VERIFY} \rangle$ successfully rectifies the identified causal disruption, returning a binary score that is averaged across step pairs. The CRMed dataset augments existing benchmarks with three annotation layers: fine-grained anatomical localiza-

tion (bounding boxes), structured causal chains (SCM), and reconstructed variants ($\mathcal{D}_{\text{shortcut}}$, $\mathcal{D}_{\text{partial}}$).

The Evaluation metrics spanning three categories: (1) *Linguistic and answer quality*: BLEU-1, F1-score, Recall, BertScore and Accuracy (Acc) assess textual fluency and answer correctness; (2) *Spatial accuracy*: IoU, Region Accuracy, Object-F1, and Region-F1 quantify localization precision; (3) *Multimodal alignment*: Align-F1 and Align Accuracy measure visual-textual correspondence. Moreover, *Hallucination Rate* calculates the fraction of generated entities absent from image and ground-truth.

4.2. Main Results

4.2.1. Region-Centric Spatial Reasoning

Table 1 evaluates bidirectional region-text alignment. MedCausalX achieves best performance on 16 of 18 metrics across structure/lesion identification and single-/multi-region detection. Notably, we attain 29.83% Region-F1 on multi-region detection, outperforming both general and

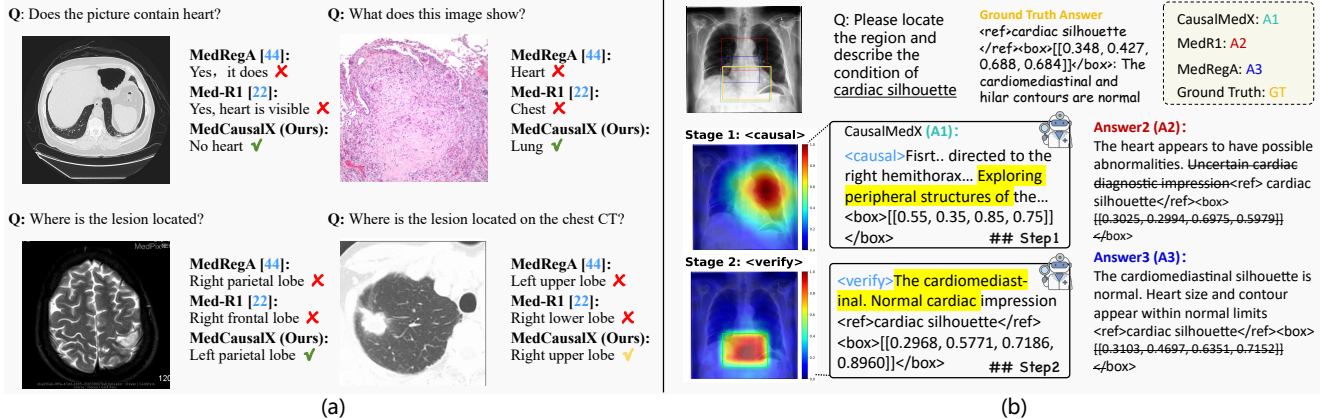


Figure 3. Comparison of causal reasoning in medical VQA and region-grounded diagnosis. (a) MedRegA and Med-R1 exhibit spurious correlations and mistakes, while MedCausalX captures correct predictions via structured causal decomposition. (b) Two-stage adaptive causal reasoning and verification, producing refined bounding boxes and logically consistent diagnostic descriptions. Attention maps are used to visualize the model’s focus. GT: ground truth; A1–A3: predictions from MedCausalX, Med-R1, and MedRegA, respectively.

medical VLMs. This stems from causal decomposition that enforces anatomical localization prior to pathological characterization, rather than relying on shortcut correlations. While MedRegA maintains text fluency advantages, our method surpasses it in spatial grounding (F1: +8.59%), revealing that previous models prioritize linguistic plausibility whereas our causal supervision enforces faithful spatial-semantic correspondence crucial in multi-lesion scenarios.

4.2.2. Medical VQA with Causal Reasoning

Table 2 demonstrates MedCausalX’s consistent superiority across four medical VQA benchmarks. Compared to MedVLM-R1, our method achieves notable improvements in accuracy (81.2% vs 79.1%) and reduces hallucination rate (47.1%→36.4%). Trajectory-level optimization prevents contradictions between intermediate steps and final predictions. Even fine-tuned CoT models like MedCoT exhibit high hallucination, confirming that conventional sequential reasoning cannot suppress spurious correlations. Training with CRMed effectively discriminates genuine causal dependencies from dataset artifacts, while structured causal factorization grounds predictions in precise anatomical evidence rather than global image statistics.

4.2.3. Grounded Report Generation

Table 3 evaluates MIMIC-CXR report generation. We achieve 37.18% BLEU-1, substantially outperforming MedRegA across linguistic, spatial, and alignment metrics. Causal factorization successfully bridges visual evidence and textual generation, while trajectory-level optimization ensures anatomically grounded descriptions rather than linguistically fluent but spatially inconsistent reports. This demonstrates that MedCausalX generalizes to X-ray report generation with precise spatial grounding, highlighting the

Table 3. Performance comparison on chest X-ray report generation benchmark. Our method employs two-stage causal reasoning with adaptive verification based on MedCausalX-32B model. Best results are highlighted in **bold**, second-best are underlined.

Method	BLEU-1	Region Acc	Align Acc	IoU
Qwen2.5-VL [2]	18.43	22.30	8.15	17.45
InternVL [11]	19.46	57.00	12.00	38.00
Med-Flamingo [56]	21.67	-	-	-
MedDr [21]	31.27	-	-	-
MedRegA [74]	<u>33.18</u>	<u>76.59</u>	<u>62.29</u>	<u>52.07</u>
MedCausalX	37.18	81.12	67.38	55.71

Table 4. Systematic ablation of core components and training stage variants on MIMIC-CXR benchmark evaluates each module’s contribution to causal reasoning and verification capabilities.

Configuration	BLEU-1	Region Acc	Align Acc	IoU
MedCausalX (Full)	37.18	81.12	67.38	55.71
<i>Main Component Ablation</i>				
✗ CRMed Dataset	26.47	41.20	18.35	26.55
✗ Reflective Tokens	29.93	51.20	32.50	38.46
✗ Causal SFT	26.02	43.80	21.75	28.55
✗ RL Training	26.96	63.50	47.30	38.09
✗ Error Collection	32.02	75.20	58.45	49.55
<i>Training Stage Variants</i>				
Base Model	23.15	35.00	12.00	24.49
+ Causal SFT	32.45	58.30	41.25	38.62
+ DPO	35.62	78.30	63.20	52.09
+ GRPO	37.18	81.12	67.38	55.71

transferability of its causal reasoning framework.

4.3. Indepth Case Analysis

Figure 3 demonstrates MedCausalX’s superior causal reasoning through contrastive examples. Panel (a) reveals baseline failures: MedRegA misidentifies anatomical struc-

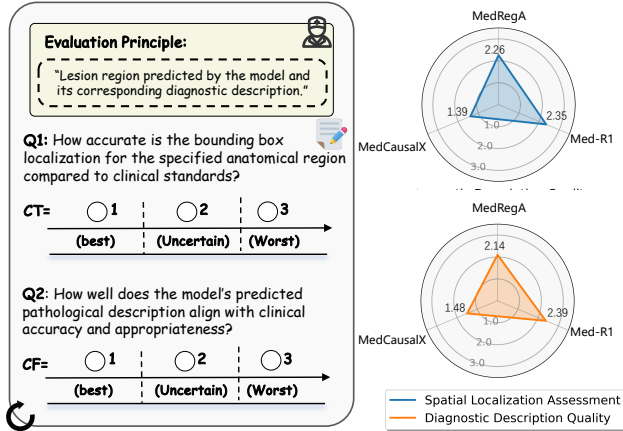


Figure 4. Radiologists’ evaluation and comparative results. Left: 3-point clinical criteria for spatial localization (Q1), diagnostic description (Q2). Right: radar chart comparing MedRegA, Med-R1, and MedCausalX on localization (blue) and description (orange); lower scores indicate better performance.

tures via global pattern matching, while Med-R1 produces spatially inconsistent localizations. MedCausalX correctly rejects spurious associations through structured $A \rightarrow P \rightarrow Y$ decomposition. Panel (b) visualizes our reflection mechanism with attention heatmaps and reasoning trajectories. The $\langle \text{causal} \rangle$ token initiates preliminary spatial analysis on relevant anatomical regions, and subsequent $\langle \text{verify} \rangle$ invocation refines localization with causally coherent descriptions. This dynamic correction, absent in static chain-of-thought baselines, enables adaptive error detection and grounds reasoning in genuine anatomical evidence rather than superficial image patterns.

4.4. Medical Expert Evaluation

We conducted an expert evaluation with board-certified radiologists with over 20 years of experience, assessing model outputs for X-ray report grounding (Section 4.2.3) on standardized 3-point scales for spatial localization and diagnostic quality. The evaluation protocol (left panel) was designed to reflect clinical practice, with stringent criteria for anatomical precision and pathological characterization. Radar chart analysis (right panel) reveals MedCausalX’s superior performance, with mean scores of 1.39 for spatial localization and 1.48 for diagnostic quality. The results provide strong expert endorsement, confirming that explicit causal factorization yields outputs that are both anatomically precise and diagnostically coherent, supporting the reliability of our causal reasoning framework.

4.5. Ablation Studies

Component Contributions. Table 4 quantifies each module’s impact. Removing CRMed causes severe degradation

Table 5. Hyperparameter sensitivity analysis. Selected configuration (shaded) achieves optimal balance across metrics.

Param.	BLEU-1	Region Acc	Align Acc	IoU
<i>Error Localization Threshold (τ)</i>				
$\tau = 0.5$	33.47	77.85	63.91	52.74
$\tau = 0.6$	35.12	79.67	66.24	54.83
$\tau = 0.7$ (default)	37.18	81.12	67.38	55.71
$\tau = 0.8$	33.23	80.17	65.82	54.96
$\tau = 0.9$	34.91	80.34	61.15	52.68
<i>GRPO Group Size (G)</i>				
$G = 4$	33.84	78.92	64.67	53.29
$G = 8$ (default)	37.18	81.12	67.38	55.71
$G = 16$	36.75	80.53	68.19	55.14
$G = 32$	34.91	79.28	65.43	53.85

(BLEU-1: 37.18→26.47), confirming structured causal supervision is indispensable for learning genuine $A! \rightarrow !P! \rightarrow !Y$ dependencies. Excluding reflective tokens reduces performance to 29.93%, as static pipelines cannot adaptively invoke verification. Ablating RL training shows supervised learning alone cannot distinguish causally valid from spurious chains. Progressive stages reveal complementary roles: Causal SFT establishes foundations, while two-stage RL exploits collected errors for stable off-policy learning and further performs adaptive exploration.

Hyperparameter Robustness Analysis. Table 5 examines key parameter sensitivity. The error localization threshold τ follows an inverted-U pattern. Overly sensitive detection with $\tau = 0.5$ introduces false positives that corrupt preference pairs, whereas conservative thresholds with $\tau = 0.9$ miss subtle errors. The optimal value of $\tau = 0.7$ balances precision and recall. For the GRPO group size G , a value of 8 balances variance reduction and computational cost. Smaller groups tend to underestimate advantages, while larger groups lead to diminishing returns. Stability across $G \in [8, 16]$ demonstrates practical robustness and indicates that minimal tuning is required for deployment.

5. Conclusion

This paper presents MedCausalX, a framework that explicitly models causal reasoning in medical vision-language inference. By combining causal factorization ($A \rightarrow P \rightarrow Y$), a reflective token architecture, and dual-policy optimization combining off-policy with on-policy RL, MedCausalX shifts from correlation-driven inference to verifiable reasoning chains. Experiments show its adaptive reflection mechanism enables dynamic error detection and correction, outperforming existing medical CoT methods in localization, diagnostic consistency, and hallucination reduction. Training with reconstructed $\mathcal{D}_{\text{shortcut}}$ and $\mathcal{D}_{\text{partial}}$ effectively distinguishes genuine causal dependencies from spurious correlations, highlighting the necessity of causal supervision in trustworthy clinical multimodal systems.

6. Additional Implementation Details

6.1. Detailed Experimental Configuration

MedCausalX employs Qwen2.5-VL-32B [2] as the base architecture with parameter-efficient LoRA adaptation targeting query, key, and value projection layers. Data augmentation preserves diagnostic integrity through random rotation ($\pm 15^\circ$), horizontal flipping (probability 0.5), brightness/contrast adjustment ($\pm 20\%$), and Gaussian noise injection ($\sigma = 0.03$). The framework augments vocabulary with reflective tokens $\langle \text{CAUSAL} \rangle$ and $\langle \text{VERIFY} \rangle$, enabling all training samples to follow unified structure $(I, q, \langle \text{CAUSAL} \rangle, R^{\text{biased}}, \langle \text{VERIFY} \rangle, R^{\text{gold}}, y)$ for learning adaptive verification through reasoning trajectories.

Training proceeds through two-stage optimization following preliminary supervised fine-tuning. Stage I (Causal SFT) maximizes joint likelihood over anatomical localization, causal chains, and diagnostic predictions for 3 epochs using AdamW with learning rate $\eta = 1 \times 10^{-6}$, weight decay 5×10^{-5} , gradient clipping threshold 1.0, and 500-step linear warmup followed by cosine annealing. Stage II integrates dual-policy refinement: off-policy DPO [64] over 2 epochs with KL coefficient $\beta = 0.1$ leverages error trajectories where semantic similarity threshold $\tau = 0.7$ identifies failure points t_{fail} via $\mathcal{S}(Y_{\text{err}}^t, Y_{\text{gt}}^t)$ comparison, constructing preference pairs contrasting erroneous continuations against correct trajectories; on-policy GRPO [68] over 2000 steps samples $G = 8$ trajectories per input, computing group-relative advantages $A^{(g)} = (R^{(g)} - \bar{R}) / (\sigma_R + \epsilon)$ with stability constant $\epsilon = 1 \times 10^{-8}$. Distributed training across 6 NVIDIA A100 (40GB) GPUs with gradient accumulation (4 steps) and mixed precision (bfloat16) converges within approximately 56 hours per dataset using 5-fold cross-validation with stratified 8:1:1 splits. Table 6 details the complete configuration.

6.2. Benchmark Dataset Statistics

We evaluate MedCausalX on established medical imaging benchmarks spanning multiple modalities and clinical domains. *MIMIC-CXR* [32] provides 377,110 chest radiographs from 227,835 imaging studies with free-text reports and 14 pathology labels for report generation tasks. *SLAKE* [44] contains 642 multi-modal images with 14,028 question-answer pairs across anatomy, modality, and pathology categories. *VQA-RAD* [36] includes 315 radiology images with 3,515 QA pairs emphasizing clinical reasoning. *PathVQA* [22] comprises 32,799 pathology images with 6,719 QA pairs for histopathological interpretation. *SA-Med2D-20M* [91] offers 4.6 million 2D medical images with 19.7 million segmentation masks across 10 modalities and 31 organs, enabling region-centric tasks including structure identification and lesion localization with bounding box annotations. All experiments employ 5-fold

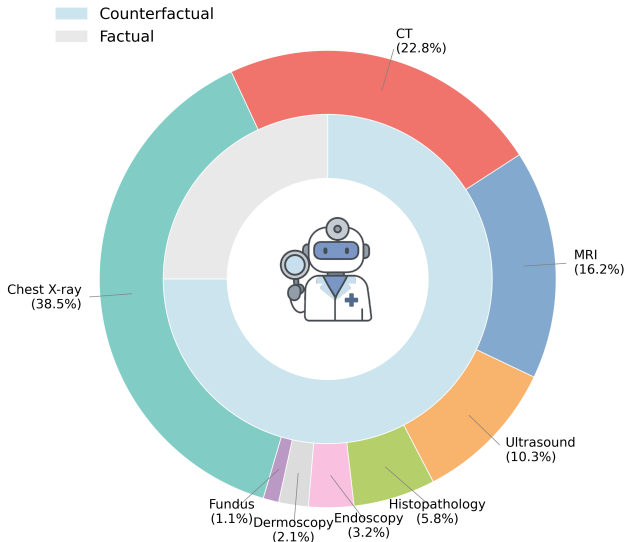


Figure 5. Modality distribution and factual-counterfactual composition of CRMed dataset. The dataset spans multiple imaging modalities with constructed counterfactual variants through controlled interventions, enabling robust causal reasoning evaluation.

cross-validation using stratified 8:1:1 train-validation-test splits for statistical reliability.

CRMed Dataset Construction. The CRMed dataset augments existing benchmarks with two systematic annotation layers. *First*, we select images from SA-Med2D-20M and MIMIC-CXR based on multi-criteria quality assessment: (i) sufficient image resolution ($\geq 512 \times 512$ pixels) and contrast quality ($\text{SNR} > 15\text{dB}$), (ii) presence of diagnostically relevant anatomical structures confirmed through clinical relevance scoring ($\geq 4/5$ by three board-certified radiologists). Selected images include bounding box annotations in format $(x_{\min}, y_{\min}, x_{\max}, y_{\max})$ covering target anatomical structures. *Second*, counterfactual variants generate $\mathcal{D}_{\text{shortcut}}$ via spatial perturbations (random shifts ± 50 pixels, scale jittering $\times [0.8, 1.2]$) disrupting $A \rightarrow P$ dependencies, and $\mathcal{D}_{\text{partial}}$ through pathology misalignment breaking $P \rightarrow Y$ causal flow while preserving image content. Intervention quality is validated by ensuring $\text{IoU} > 0.7$ between perturbed and original bounding boxes to maintain anatomy. The resulting corpus contains 89,342 images with 267,128 causal samples, averaging 4.2 reasoning steps per chain ($\text{SD}=1.3$). Modality distribution spans chest X-ray (38.5%), CT (22.8%), MRI (16.2%), ultrasound (10.3%), histopathology (5.8%), endoscopy (3.2%), dermoscopy (2.1%), and fundus (1.1%), with counterfactual plausibility scores > 0.85 via GPT-4V evaluation.

Table 6. Complete hyperparameter configuration for MedCausalX training and inference.

Hyperparameter	Value
Base Model	Qwen2.5-VL-32B
LoRA Rank (r)	64
LoRA Alpha (α)	128
LoRA Dropout	0.05
Target Modules	q-proj, k-proj, v-proj
Reflective Tokens	\langle CAUSAL \rangle , \langle VERIFY \rangle
Nucleus Sampling (p)	0.9
Temperature (T)	0.7
Batch Size	64
Max Tokens (T_{\max})	2048
<i>Causal SFT (Stage I)</i>	
Epochs	3
Optimizer	AdamW
Learning Rate (η)	1×10^{-6}
Weight Decay	5×10^{-5}
Gradient Clipping	1.0
Warmup Steps	500
LR Schedule	Linear + Cosine
<i>Dual-Policy Optimization (Stage II)</i>	
Off-policy training:	
Epochs	2
KL Coefficient (β)	0.1
Error Threshold (τ)	0.7
On-policy training:	
Training Steps	2000
Group Size (G)	8
Stability Constant (ϵ)	1×10^{-8}
<i>Infrastructure</i>	
GPUs	$6 \times$ A100 (40GB)
Gradient Accumulation	4 steps
Mixed Precision	bfloat16
Training Time	\sim 72 hours/dataset
Cross-validation	5-fold
Data Split	8:1:1

7. Additional Experimental Results

7.1. Causal Reasoning Cases

MedCausalX demonstrates robust causal reasoning across multiple public medical VQA datasets. In Figure 9 (Case 1), the model successfully performs multi-object anatomical quantification, accurately identifying bilateral pulmonary structures via causal factorization. Figure 10 (Case 2) illustrates its capability in anatomical landmark detection, where the presence of the gastric cardia is correctly confirmed through systematic spatial reasoning. In Figure 11 (Case 3), MedCausalX shows precise spatial localization by identifying an endocardial lesion adjacent to the lower intra-ventricular septum, leveraging structured anatomical factor-

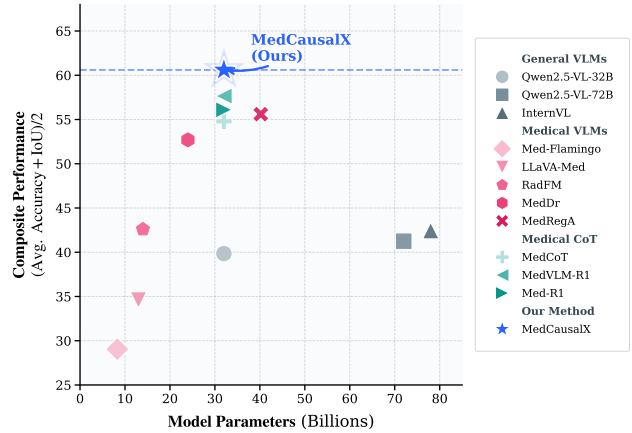


Figure 6. Comparison of model efficiency and performance across medical VLMs. MedCausalX achieves the highest composite score at 32B parameters, demonstrating superior causal reasoning capabilities while maintaining computational efficiency.

ization ($A \rightarrow P \rightarrow Y$). Finally, Figure 12 (Case 4) demonstrates binary anatomical detection, with the model reliably confirming uterine presence through causal verification. Together, these examples highlight that MedCausalX grounds its diagnostic predictions in genuine anatomical evidence, rather than relying on superficial pattern correlations.

7.2. Prompt Engineering and Reflective Tokens

MedCausalX utilizes a structured prompt template (Figure 8) to guide causal reasoning through explicit task decomposition. The system prompt directs the model to systematically examine medical images, compare findings with initial predictions, and link observations to the provided concept vocabulary using concrete visual evidence. This hierarchical framework ensures semantic consistency with medical ontologies while producing declarative sentences suitable for causal verification. Reflective tokens \langle causal \rangle and \langle verify \rangle facilitate dynamic reasoning mode transitions, allowing preliminary anatomical analysis to trigger subsequent verification and correction phases whenever inconsistencies are detected.

7.3. Efficiency-Performance Analysis

Figure 6 compares efficiency and performance of state-of-the-art medical vision-language models using a composite score averaging diagnostic accuracy and spatial grounding IoU. General-purpose VLMs improve modestly with scale but remain below medical-specific models. Domain-adapted medical VLMs achieve higher performance, and chain-of-thought enhanced models further benefit from structured reasoning. MedCausalX sets a new state-of-the-art, outperforming comparable 32B models and even larger specialized systems while using fewer parameters. These

Table 7. Model scaling analysis across region-centric medical reasoning tasks. We evaluate MedCausalX variants with 3B, 14B, and 32B parameters to assess the impact of model capacity on causal reasoning performance. Best results are highlighted in **bold**, second-best are underlined. All models trained with identical data and optimization strategies.

Model Scale	Region-to-Text Identification										Text-to-Region Detection							
	Structure Identification					Lesion Identification					Single-Region Detection				Multi-Region Detection			
	BLEU-1	F1	Recall	BertScore	Acc	BLEU-1	F1	Recall	BertScore	Acc	Obj-F1	Reg-F1	Align-F1	IoU	Obj-F1	Reg-F1	Align-F1	IoU
MedCausalX-3B	53.42	54.68	55.20	52.15	48.20	38.29	39.12	40.35	48.65	35.12	68.45	21.47	18.23	24.49	55.18	14.23	12.47	19.82
MedCausalX-14B	<u>73.49</u>	<u>74.23</u>	<u>75.80</u>	<u>54.20</u>	<u>55.30</u>	<u>56.43</u>	<u>57.80</u>	<u>59.25</u>	<u>70.83</u>	<u>52.80</u>	<u>79.82</u>	<u>34.62</u>	<u>28.15</u>	<u>33.75</u>	<u>65.75</u>	<u>19.56</u>	<u>17.85</u>	<u>26.18</u>
MedCausalX-32B	79.82	80.15	81.25	88.45	70.15	63.27	64.35	65.80	81.90	61.35	82.45	46.82	44.92	44.35	72.38	29.51	26.82	35.76

Table 8. Model scale and architecture comparison across medical VQA benchmarks. Light blue background indicates selected configuration.

Model	VQA-RAD	SLAKE	PathVQA	PMC-VQA	Average
<i>Vision-Language Models (Zero-shot)</i>					
LLaVA-1.5-13B [48]	53.2	58.5	52.8	56.3	55.2
InternVL-2-40B [11]	59.8	65.2	61.5	67.1	63.4
MedRegA-40B [74]	76.9	84.1	68.5	79.5	77.3
<i>Medical CoT Methods (Qwen2.5-VL-32B Backbone)</i>					
Med-R1 [35]	76.9	85.4	69.5	81.9	78.4
MedVLM-R1 [59]	77.3	85.7	70.8	82.4	79.1
<i>MedCausalX Scale Variants (Qwen2.5-VL Backbone)</i>					
MedCausalX-3B	67.8	75.9	62.5	68.2	68.6
MedCausalX-7B	73.5	81.8	67.3	74.9	74.4
MedCausalX-32B	79.8	87.2	73.2	84.6	81.2

Table 9. Ablation study on training strategy configuration. Light blue background indicates selected configuration, bold values denote best performance in each row.

Config.	Value	VQA-RAD	SLAKE	PathVQA	PMC-VQA	Average
<i>(a) Training Stage Order</i>						
Seq.	GRPO→DPO	73.5	81.4	68.2	78.9	75.5
	DPO→GRPO	79.8	87.2	73.2	84.6	81.2
<i>(b) GRPO Group Size G</i>						
G	4	76.8	84.3	70.5	81.7	78.3
	6	78.5	86.1	72.1	83.5	80.1
	8	79.8	87.2	73.2	84.6	81.2
	12	78.9	88.5	72.6	83.9	80.9
	16	77.4	85.2	71.3	82.4	79.1

results highlight that explicit causal reasoning and structured factorization provide substantial gains beyond raw parameter scaling, establishing MedCausalX as the most efficient and effective solution in its class.

7.4. MedCausalX Scaling Analysis

Table 7 examines how model capacity influences causal reasoning across region-centric medical tasks. The 3B variant captures basic anatomical structures but still shows notable limitations in lesion-level reasoning, achieving only 53.42% BLEU-1 for structure identification. Scaling to 14B parameters significantly improves performance by approximately 20 points, indicating enhanced causal decomposition and a more robust hierarchical understanding of medical concepts. The 32B variant achieves the best overall perfor-

mance, with BLEU-1 of 79.82% and BertScore of 88.45%, demonstrating superior semantic coherence, precise spatial grounding, and consistent reasoning quality. These trends confirm that larger models enable deeper causal verification and stronger spatial-linguistic alignment, validating MedCausalX’s scalable and versatile architecture for handling complex medical reasoning scenarios.

7.5. Model Architecture Effect

Table 8 highlights how architectural design and model capacity affect VQA reasoning. MedCausalX-32B achieves 81.2% average accuracy, outperforming CoT baselines Med-R1 and MedVLM-R1 by 2–3 points, demonstrating that its causal factorization and error-attributed reinforcement learning architecture enables structured reasoning beyond standard chain-of-thought. Performance scales from 68.6% at 3B to 81.2% at 32B, showing that counterfactual reasoning benefits from increased capacity. General VLMs LLaVA-1.5 (55.2%) and InternVL-2 (63.4%) lag behind, emphasizing the importance of specialized architecture for anatomically grounded diagnostic tasks.

7.6. Training Strategy Ablation

Table 9 validates our dual-stage reinforcement learning design. The DPO→GRPO sequence achieves 81.2% average accuracy, outperforming the reversed order by 5.7 points. This indicates that applying DPO first allows off-policy learning from error trajectories, effectively establishing robust reasoning foundations, while subsequent GRPO exploration refines causal intervention strategies without premature convergence to superficial patterns. Regarding group size configuration, $G=8$ provides an optimal balance: smaller groups introduce excessive gradient noise that destabilizes causal learning, whereas larger configurations, such as $G=12$ or 16, exhibit diminishing returns because conservative advantage normalization suppresses the discovery of novel interventions, which is essential for adaptive and flexible reasoning.

7.7. Reward Component Configuration

Table 10 highlights the interdependence of reward components in causal reasoning optimization. Balanced weighting achieves the best accuracy, outperforming accuracy-only

Table 10. Ablation of reward components and error localization threshold. Light blue background indicates selected configuration.

Config.	Value	VQA-RAD	SLAKE	PathVQA	PMC-VQA	Average
<i>(a) Reward Weight Configuration $\lambda_{acc}/\lambda_{causal}$</i>						
λ	1.0/0.0	71.5	78.9	65.3	76.2	73.0
	0.7/0.3	76.8	84.1	70.5	81.7	78.3
	0.5/0.5	79.8	87.2	73.2	84.6	81.2
	0.3/0.7	78.2	85.7	71.8	83.1	79.7
	0.0/1.0	67.3	74.5	61.2	71.8	68.7
<i>(b) Error Localization Threshold τ</i>						
τ	0.3	70.8	77.5	64.1	75.3	71.9
	0.5	75.3	82.9	69.4	80.5	77.0
	0.7	79.8	87.2	73.2	84.6	81.2
	0.8	77.1	84.6	70.8	82.3	78.7
	0.9	72.4	79.8	66.5	77.1	73.9

Table 11. Out-of-domain evaluation on specialized medical VQA datasets. Models trained on core benchmarks and evaluated zero-shot on unseen domains.

Method	OVQA	EndoVis-VQA	Skin-VQA	Average
GPT-4o [27]	43.5	39.8	46.1	43.1
LLaVA-Med [37]	47.2	44.3	49.5	47.0
InternVL-2 [11]	49.8	46.7	51.2	49.2
Med-R1 [35]	44.8	40.5	46.3	43.9
MedVLM-R1 [59]	50.3	47.1	49.8	49.1
MedCausalX (Ours)	58.4	54.2	59.7	57.4

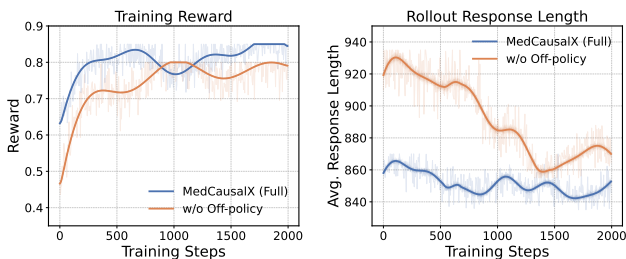


Figure 7. Training dynamics of on-policy GRPO optimization. MedCausalX (Full) with DPO pretraining achieves higher rewards and maintains stable, compact reasoning compared to direct GRPO training from preliminary SFT baseline.

and causal-only setups, showing that multi-objective optimization prevents overfitting to diagnostic shortcuts while preserving reasoning quality. For error localization threshold τ , our study shows that 0.7 provides the best trade-off between sensitivity and specificity: lower thresholds generate excessive false positives, while higher thresholds miss critical reasoning errors, confirming that precise error attribution is essential for effective causal training.

7.8. Cross-Dataset Generalization

Table 11 demonstrates MedCausalX’s superior zero-shot transfer across specialized medical domains. The model achieves an average accuracy of 57.4%. Gains are partic-

ularly notable on domain-specific tasks, including OVQA in ophthalmology with an improvement of 8.1% and Skin VQA in dermatology with an improvement of 9.9%. These results suggest that causal reasoning mechanisms, such as anatomical localization, pathology identification, and counterfactual verification, provide structural inductive biases that generalize effectively across modalities and anatomical regions. In contrast, reasoning-enhanced methods like Med-R1 and MedVLM-R1 achieve only modest improvements over standard models such as InternVL-2, indicating that chain-of-thought approaches lack sufficient compositional structure for reliable domain generalization.

7.9. Training Dynamics Analysis

Figure 7 illustrates the training dynamics of MedCausalX during on-policy GRPO optimization. The reward curves show steady improvement for both configurations, with MedCausalX (Full) benefiting from off-policy initialization to start higher. While the w/o Off-policy baseline gradually catches up, the Full version maintains a consistent advantage, reaching 0.845 versus 0.791, a 5.4-point gap. Rollout response lengths reveal distinct trajectories: MedCausalX (Full) maintains stable, compact reasoning around 850 tokens throughout training, reflecting DPO’s pre-established efficiency. In contrast, the w/o Off-policy baseline exhibits a pronounced learning curve, starting at 919 tokens and ultimately stabilizing around 870 tokens as GRPO converges. These patterns confirm that off-policy training provides immediate efficiency benefits, while direct GRPO requires longer optimization to achieve comparable compactness.

Prompt Templates

```

{
  "system_prompt": {
    "role": "system",
    "content": "You are an expert medical image analysis assistant with causal reasoning capabilities. Your task is to analyze medical images through structured causal decomposition following the A→P→Y (Anatomy→Pathology→Diagnosis) framework.

    1. Task Description: Examine medical images using causal factorization. Begin with precise anatomical localization (A), proceed to pathological characterization (P), and conclude with diagnostic inference (Y). Each stage must be causally grounded in the preceding observations.

    2. Reasoning Protocol: Employ two-stage reflective reasoning:
      - Stage 1 (<causal>): Generate preliminary causal analysis by systematically identifying anatomical structures, describing their spatial relationships, and linking visual features to pathological concepts. Provide bounding box coordinates [x1, y1, x2, y2] in normalized 0-1 range for all anatomical references.
      - Stage 2 (<verify>): Critically evaluate the initial causal chain for spurious correlations or logical inconsistencies. Refine anatomical localization, verify pathological characterizations against visual evidence, and correct any causal disruptions in the reasoning trajectory.

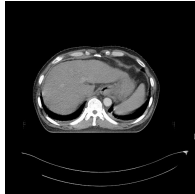
    3. Causal Chain Construction: For each reasoning stage, explicitly state:
      - Anatomical Observation: \"The <ref>structure_name</ref> <box>[x1,y1,x2,y2]</box> exhibits [specific features]\"
      - Pathological Inference: \"Based on [anatomical evidence], the pathological manifestation indicates [finding]\"
      - Diagnostic Conclusion: \"The causal chain establishes: [A→P→Y relationship]\"

    4. Output Format: Structure your response using reflective tokens:
      <causal>
      [Preliminary anatomical localization and initial pathological characterization with detailed spatial annotations]
      <verify>
      [Critical evaluation of causal dependencies, refinement of spatial localization, and correction of spurious associations]

    5. Causal Verification Principles:
      - Reject diagnoses based solely on global image statistics without anatomical grounding
      - Distinguish genuine causal dependencies from confounding correlations
      - Ensure spatial consistency between anatomical claims and bounding box coordinates
      - Validate that pathological characterizations logically follow from observed anatomical features"
  },
  "user_prompt": {
    "role": "user",
    "content": [
      {
        "type": "image",
        "image": " /path/to/medical_image.jpg "
      },
      {
        "type": "text",
        "text": "What pathological findings are present in this image?"
      }
    ]
  }
}

```

Figure 8. Structured prompt template for MedCausalX showing system instructions for pathological analysis approach and output format specifications enabling causal chain generation.



Case 1

Q: How many lungs are shown in this image?

<causal> This is a frontal chest radiograph displaying thoracic anatomy. I observe bilateral radiolucent lung fields extending from the apices to the diaphragmatic surfaces. The **<ref>left lung</ref>** **<box>[0.52, 0.25, 0.85, 0.68]</box>** demonstrates characteristic vascular markings extending throughout the pulmonary parenchyma with preserved aeration. The cardiac silhouette occupies the expected left-sided position. Moving to the contralateral side, the **<ref>right lung</ref>** **<box>[0.15, 0.28, 0.48, 0.72]</box>** exhibits similar radiolucency with clearly demarcated costophrenic angles and hemidiaphragm interfaces. Both lung fields maintain symmetric expansion patterns without evidence of consolidation, atelectasis, or pleural effusion. The mediastinal contours remain centered with preserved hilar structures bilaterally. **## Step1**

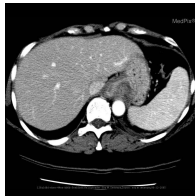
<verify> I need to confirm accurate enumeration and spatial boundary verification. Systematic examination validates two distinct anatomical units: the right pulmonary structure demonstrating three-lobed configuration and the left pulmonary structure with two-lobed morphology, both separated by the central mediastinum. The **<ref>right hemithorax</ref>** **<box>[0.10, 0.22, 0.50, 0.75]</box>** contains one complete lung unit with visible fissural margins, while the **<ref>left hemithorax</ref>** **<box>[0.50, 0.20, 0.88, 0.70]</box>** contains the second complete lung unit. No supernumerary pulmonary structures, accessory lobes, or congenital variants are present. Anatomical assessment identifies the bilateral thoracic cavities, and pathological evaluation demonstrates normally aerated pulmonary parenchyma, confirming the diagnostic conclusion of exactly two lungs.

Answer: 2



Step2

Figure 9. Chest radiograph demonstrating bilateral lung detection where MedCausalX accurately quantifies two distinct pulmonary structures through structured anatomical enumeration and spatial boundary verification.



Case 2

Q: Does this plane of section include the gastric cardia?

<causal> This axial contrast-enhanced CT section traverses the upper abdomen at the level of the gastroesophageal junction. I identify the **<ref>gastric fundus</ref>** **<box>[0.38, 0.35, 0.62, 0.68]</box>** as a gas-filled hollow viscus structure in the left upper quadrant with characteristic mucosal folds. Adjacent to this, at the anatomical transition zone where the esophagus penetrates the diaphragmatic hiatus, I observe the **<ref>gastric cardia region</ref>** **<box>[0.42, 0.38, 0.58, 0.52]</box>** demonstrating the proximal gastric pouch immediately inferior to the esophagogastric junction. The cardia represents the anatomical segment receiving esophageal contents, positioned at the gastric inlet where stratified squamous epithelium transitions to columnar mucosa. The imaging plane clearly captures this critical anatomical landmark with preserved wall thickness and no evidence of hiatal hernia displacement. **## Step1**

<verify> I need to confirm definitive cardia inclusion within this imaging section. Careful and systematic evaluation of the relevant anatomical structures demonstrates their expected spatial relationships and continuity. The distal esophagus descends smoothly through the esophageal hiatus, maintaining its normal caliber and orientation, while the gastroesophageal junction clearly marks the Z-line transition, delineating the boundary between esophageal and gastric mucosa. Immediately caudal lies the **<ref>proximal gastric cardia</ref>** **<box>[0.40, 0.42, 0.60, 0.56]</box>** before the fundic expansion. The hepatogastric ligament insertion and left gastric artery origin provide additional confirmation of cardia localization. The causal chain establishes that anatomical localization identifies the gastroesophageal transition zone, pathological characterization confirms intact mucosal architecture, and the diagnostic conclusion verifies the presence of the cardia within this section.

Answer: yes



Step2

Figure 10. Abdominal examination section validating gastric cardia identification through causal anatomical landmark detection, confirming presence via systematic spatial relationship analysis with esophagogastric junction.



Case 3

Q: What is the location of the echodense image seen in the echocardiogram?

<causal> This echocardiographic four-chamber view displays cardiac anatomy with clearly demarcated chamber boundaries and septal structures. I observe the **<ref>right atrium</ref>** **<box>[0.28, 0.15, 0.58, 0.42]</box>** in the superior right portion with the **<ref>left ventricle</ref>** **<box>[0.42, 0.52, 0.75, 0.85]</box>** occupying the inferior left quadrant. Within the cardiac septum, specifically along the **<ref>lower intraventricular septum</ref>** **<box>[0.48, 0.58, 0.62, 0.78]</box>**, I identify an echodense mass exhibiting irregular borders and heterogeneous echogenicity. This **<ref>endocardial lesion</ref>** **<box>[0.52, 0.64, 0.58, 0.72]</box>** projects into the left ventricular cavity with attachment to the septal endocardial surface, consistent with a fixed intracardiac mass rather than mobile thrombus. The lesion's position adjacent to rather than within the upper septum distinguishes it from membranous septal pathology. ## Step1

<verify> I need to precisely confirm the lesion's septal position relative to anatomical landmarks. Systematic evaluation establishes that the mass originates from the **<ref>inferior interventricular septum</ref>** **<box>[0.46, 0.60, 0.64, 0.80]</box>** below the mid-septal plane, specifically in the apical-to-mid ventricular region. The **<ref>aortic root</ref>** **<box>[0.38, 0.32, 0.52, 0.48]</box>** and mitral valve apparatus serve as superior reference points, confirming the lesion's distance from the upper septal structures. The mass demonstrates direct contact with the **<ref>lower septal myocardium</ref>** **<box>[0.50, 0.62, 0.60, 0.76]</box>** without extension to the superior membranous region. The causal chain validates that anatomical localization identifies the lower interventricular septum, pathological characterization reveals an endocardial-based echodense mass, and the diagnostic conclusion confirms the lesion's proximity to the lower, rather than the upper, septum. ## Step2

Answer: Adjacent to the lower intraventricular septum ✔

Figure 11. Echocardiographic image demonstrating successful causal localization of endocardial lesion positioned adjacent to lower intraventricular septum through structured anatomical-pathological reasoning chain.



Case 4

Q: Is uterus present?

<causal> This axial pelvic CT section demonstrates female reproductive anatomy within the true pelvis. I identify a midline soft tissue structure positioned between the **<ref>urinary bladder</ref>** **<box>[0.35, 0.32, 0.65, 0.58]</box>** anteriorly and the **<ref>rectosigmoid colon</ref>** **<box>[0.38, 0.65, 0.62, 0.85]</box>** posteriorly. This intermediate structure exhibits characteristic morphology of the **<ref>uterine corpus</ref>** **<box>[0.42, 0.45, 0.58, 0.62]</box>** with homogeneous myometrial density and preserved endometrial cavity echogenicity. The organ demonstrates typical pear-shaped configuration in the coronal plane with smooth serosal surfaces. Bilateral parametrial soft tissues and vascular pedicles provide additional anatomical confirmation. The uterus maintains normal anteverted position without evidence of surgical absence, congenital agenesis, or displacement by pelvic masses. ## Step1

<verify> I need to definitively exclude confounding structures and confirm uterine identity. Systematic evaluation eliminates alternative diagnoses: the structure's location in the **<ref>vesicouterine space</ref>** **<box>[0.40, 0.40, 0.60, 0.50]</box>** excludes bowel loops; its homogeneous density distinguishes it from vascular structures; and its characteristic shape eliminates ovarian or adnexal masses. The **<ref>cervicouterine junction</ref>** **<box>[0.44, 0.58, 0.56, 0.64]</box>** transitions into the superior vaginal fornix inferiorly, confirming anatomical continuity. Bilateral **<ref>broad ligament attachments</ref>** **<box>[0.25, 0.48, 0.75, 0.58]</box>** extend laterally toward pelvic sidewalls. The causal chain establishes that anatomical localization identifies a midline pelvic structure, pathological characterization reveals typical uterine morphology and density, and the diagnostic conclusion confirms the presence of the uterus unambiguously.
Answer: yes ## Step2

Figure 12. Pelvic CT scan validating binary anatomical detection where MedCausalX correctly confirms uterine presence through causal verification eliminating confounding structures.

References

- [1] Josh Achiam, Steven Adler, Sandhini Agarwal, Lama Ahmad, Ilge Akkaya, Florencia Leoni Aleman, Diogo Almeida, Janko Altenschmidt, Sam Altman, Shyamal Anadkat, et al. Gpt-4 technical report. *arXiv preprint arXiv:2303.08774*, 2023. 1
- [2] Shuai Bai and et al. Qwen2.5-vl: Technical report. <https://arxiv.org/abs/2502.13923>, 2025. arXiv preprint arXiv:2502.13923. 5, 6, 7, 9
- [3] Yuntao Bai, Saurav Kadavath, Sandipan Kundu, Amanda Askell, Jackson Kernion, Andy Jones, Anna Chen, Anna Goldie, Azalia Mirhoseini, Cameron McKinnon, and et al. Constitutional ai: Harmlessness from ai feedback, 2022. 3
- [4] Linqin Cai, Haodu Fang, Nuoying Xu, and Bo Ren. Counterfactual causal-effect intervention for interpretable medical visual question answering. *IEEE Transactions on Medical Imaging*, 2024. 3
- [5] Zheng Cai, Maosong Cao, Haojiong Chen, Kai Chen, Keyu Chen, Xin Chen, Xun Chen, Zehui Chen, Zhi Chen, Pei Chu, et al. Internlm2 technical report. *arXiv preprint arXiv:2403.17297*, 2024. 5
- [6] Daniel C Castro, Ian Walker, and Ben Glocker. Causality matters in medical imaging. *Nature Communications*, 11(1):3673, 2020. 2
- [7] Junying Chen, Chi Gui, Ruyi Ouyang, Anningzhe Gao, Shunian Chen, Guiming Hardy Chen, Xidong Wang, Ruifei Zhang, Zhenyang Cai, Ke Ji, et al. Huatuogpt-vision, towards injecting medical visual knowledge into multimodal llms at scale. *arXiv preprint arXiv:2406.19280*, 2024. 3
- [8] Xinyun Chen, Maxwell Lin, Nathanael Schärli, and Denny Zhou. Teaching large language models to self-debug. In *ICLR*, 2024. 2
- [9] Yihang Chen, Yanyan Huang, Fuying Wang, Maximus Yeung, Yuming Jiang, Shujun Wang, and Lequan Yu. Bridging radiology and pathology foundation models via concept-based multimodal co-adaptation. In *The Fourteenth International Conference on Learning Representations*. 1
- [10] Zhe Chen, Weiyun Wang, Hao Tian, Shenglong Ye, Zhangwei Gao, Erfei Cui, Wenwen Tong, Kongzhi Hu, Jiapeng Luo, Zheng Ma, et al. How far are we to gpt-4v? closing the gap to commercial multimodal models with open-source suites. *arXiv preprint arXiv:2404.16821*, 2024. 5
- [11] Zhe Chen, Jiannan Wu, Wenhai Wang, Weijie Su, Guo Chen, Sen Xing, Muyan Zhong, Qinglong Zhang, Xizhou Zhu, Lewei Lu, et al. Internvl: Scaling up vision foundation models and aligning for generic visual-linguistic tasks. In *Proceedings of the IEEE/CVF conference on computer vision and pattern recognition*, pages 24185–24198, 2024. 6, 7, 11, 12
- [12] Paul F Christiano, Jan Leike, Tom Brown, Miljan Martic, Shane Legg, and Dario Amodei. Deep reinforcement learning from human preferences. *Advances in neural information processing systems*, 30, 2017. 3
- [13] LIU Chuang, Hongyan Xu, Yichao Cao, Xiu Su, Zhe Qu, Tianfa Li, Shan An, and Haogang Zhu. Tinyimg: Transferring generalization from vision foundation models to single-domain medical imaging. In *Forty-second International Conference on Machine Learning*, 2025. 1
- [14] Tianchen Deng, Xuefeng Chen, Yi Chen, Qu Chen, Yuyao Xu, Lijin Yang, Le Xu, Yu Zhang, Bo Zhang, Wuxiong Huang, and Hesheng Wang. Gaussiandwm: 3d gaussian driving world model for unified scene understanding and multi-modal generation. *arXiv preprint arXiv:2512.23180*, 2025. 2
- [15] Tianchen Deng, Yue Pan, Shenghai Yuan, Dong Li, Chen Wang, Mingrui Li, Long Chen, Lihua Xie, Danwei Wang, Jingchuan Wang, Javier Civera, Hesheng Wang, and Weidong Chen. What is the best 3d scene representation for robotics? from geometric to foundation models. *arXiv preprint arXiv:2512.03422*, 2025. 2
- [16] Yihe Deng, Pan Lu, Fan Yin, Ziniu Hu, Sheng Shen, Quanquan Gu, James Zou, Kai-Wei Chang, and Wei Wang. Enhancing large vision language models with self-training on image comprehension. *Advances in Neural Information Processing Systems*, 37:131369–131397, 2024. 1
- [17] Ruiyi Ding, Yongxuan Lv, Xianhui Meng, Jiahe Song, Chao Wang, Chen Jiang, and Yuan Cheng. Prpo: Aligning process reward with outcome reward in policy optimization. *arXiv preprint arXiv:2601.07182*, 2026. 3
- [18] Rong Fu, Yiqing Lyu, Chunlei Meng, Muge Qi, Yabin Jin, Qi Zhao, Li Bao, Juntao Gao, Fuqian Shi, Nilanjan Dey, et al. Neurosymb-mrg: Differentiable abductive reasoning with active uncertainty minimization for radiology report generation. *arXiv preprint arXiv:2603.01756*, 2026. 2
- [19] Robert Geirhos, Jörn-Henrik Jacobsen, Claudio Michaelis, Richard Zemel, Wieland Brendel, Matthias Bethge, and Felix A Wichmann. Shortcut learning in deep neural networks. *Nature Machine Intelligence*, 2(11):665–673, 2020. 1, 2
- [20] Daya Guo, Dejian Yang, Haowei Zhang, Junxiao Song, Ruoyu Zhang, Runxin Xu, Qihao Zhu, Shirong Ma, Peiyi Wang, Xiao Bi, et al. Deepseek-r1: Incentivizing reasoning capability in llms via reinforcement learning. *arXiv preprint arXiv:2501.12948*, 2025. 3
- [21] Sunan He, Yuxiang Nie, Zhixuan Chen, Zhiyuan Cai, Hongmei Wang, Shu Yang, and Hao Chen. Meddr: Diagnosis-guided bootstrapping for large-scale medical vision-language learning. *arXiv preprint arXiv:2404.15127*, 2024. 5, 6, 7
- [22] Xuehai He, Zhuo Cai, Wenlan Wei, Yichen Zhang, Luntian Mou, Eric Xing, and Pengtao Xie. Pathological visual question answering. *arXiv preprint arXiv:2010.12435*, 2020. 5, 6, 9
- [23] Xinhai Hou, Shaoyuan Xu, Manan Biyani, Moyan Li, Jia Liu, Todd C Hollon, and Bryan Wang. Codev: Code with images for faithful visual reasoning via tool-aware policy optimization. *arXiv preprint arXiv:2511.19661*, 2025. 2, 3
- [24] Mingzhe Hu, Shaoyan Pan, Yuheng Li, and Xiaofeng Yang. Advancing medical imaging with language models: A journey from n-grams to chatgpt. *arXiv preprint arXiv:2304.04920*, 2023. 3
- [25] Jie Huang, Shixiang Shane Gu, Le Hou, Yuexin Wu, Xuezhi Wang, Hongkun Yu, and Jiawei Han. Large

- language models cannot self-correct reasoning yet. In *Proceedings of the International Conference on Learning Representations (ICLR) 2024*, 2024. Paper ID: 8b4add8b0aa8749d80a34ca5d941c355. 2
- [26] Yue Huang, Yanyuan Chen, Dexuan Xu, Weihua Yue, Huamin Zhang, Meikang Qiu, and Yu Huang. Medreflect: Teaching medical llms to self-improve via reflective correction. *arXiv preprint arXiv:2510.03687*, 2025. 1, 2
- [27] Aaron Hurst, Adam Lerer, Adam P Goucher, Adam Perelman, Aditya Ramesh, Aidan Clark, AJ Ostrow, Akila Welihinda, Alan Hayes, Alec Radford, et al. Gpt-4o system card. *arXiv preprint arXiv:2410.21276*, 2024. 5, 12
- [28] Songtao Jiang, Tuo Zheng, Yan Zhang, Yeying Jin, Li Yuan, and Zuozhu Liu. Med-moe: Mixture of domain-specific experts for lightweight medical vision-language models. In *Findings of the association for computational linguistics: EMNLP 2024*, pages 3843–3860, 2024. 3
- [29] Songtao Jiang, Yuan Wang, Sibao Song, Tianxiang Hu, Chenyi Zhou, Bin Pu, Yan Zhang, Zhibo Yang, Yang Feng, Joey Tianyi Zhou, et al. Hulu-med: A transparent generalist model towards holistic medical vision-language understanding. *arXiv preprint arXiv:2510.08668*, 2025. 3
- [30] Ruinan Jin, Yingbin Liang, and Shaofeng Zou. Why adam can beat sgd: Second-moment normalization yields sharper tails. *arXiv preprint arXiv:2603.03099*, 2026. 6
- [31] Ruinan Jin et al. Tic-grpo: Provable and efficient optimization for reinforcement learning from human feedback. 3
- [32] Alistair EW Johnson, Tom J Pollard, Seth J Berkowitz, Nathaniel R Greenbaum, Matthew P Lungren, Chih-ying Deng, Roger G Mark, and Steven Horng. Mimic-cxr, a de-identified publicly available database of chest radiographs with free-text reports. *Scientific data*, 6(1):317, 2019. 5, 9
- [33] Takeshi Kojima, Shixiang Shane Gu, Machel Reid, Yutaka Matsuo, and Yusuke Iwasawa. Large language models are zero-shot reasoners. *Advances in Neural Information Processing Systems*, 35:22199–22213, 2022. 2
- [34] Aviral Kumar, Vincent Zhuang, Rishabh Agarwal, Yi Su, John D. Co-Reyes, Avi Singh, Kate Baumli, Shariq Iqbal, Colton Bishop, Rebecca Roelofs, Lei M. Zhang, Kay McKinney, Disha Shrivastava, Cosmin Paduraru, George Tucker, Doina Precup, Feryal Behbahani, and Aleksandra Faust. Training language models to self-correct via reinforcement learning. 2024. 2
- [35] Yuxiang Lai, Jike Zhong, Ming Li, Shitian Zhao, Yuheng Li, Konstantinos Psounis, and Xiaofeng Yang. Med-r1: Reinforcement learning for generalizable medical reasoning in vision-language models. *IEEE Transactions on Medical Imaging*, 2026. 1, 2, 3, 5, 6, 11, 12
- [36] Jason J Lau, Soumya Gayen, Asma Ben Abacha, and Dina Demner-Fushman. A dataset of clinically generated visual questions and answers about radiology images. *Scientific data*, 5(1):1–10, 2018. 5, 6, 9
- [37] Chunyuan Li, Cliff Wong, Sheng Zhang, Naoto Usuyama, Haotian Liu, Jianwei Yang, Tristan Naumann, Hoifung Poon, and Jianfeng Gao. Llava-med: Training a large language-and-vision assistant for biomedicine in one day. *Advances in Neural Information Processing Systems*, 36: 28541–28564, 2023. 5, 6, 12
- [38] Long Li, Jiaran Hao, Jason Klein Liu, Zhijian Zhou, Yanting Miao, Wei Pang, Xiaoyu Tan, Wei Chu, Zhe Wang, Shirui Pan, et al. The choice of divergence: A neglected key to mitigating diversity collapse in reinforcement learning with verifiable reward. *arXiv preprint arXiv:2509.07430*, 2025. 3
- [39] Yuqi Li, Junhao Dong, Chuanguang Yang, Shiping Wen, Piotr Koniusz, Tingwen Huang, Yingli Tian, and Yew-Soon Ong. Mmt-ard: Multimodal multi-teacher adversarial distillation for robust vision-language models. *arXiv preprint arXiv:2511.17448*, 2025. 3
- [40] Yuqi Li, Hansheng Zeng, Fuyan Zhang, Chuanguang Yang, Yanli Li, and Weiping Ding. Efficient Medical Image Segmentation via Reinforcement Learning-Driven K-Space Sampling. *IEEE Transactions on Emerging Topics in Computational Intelligence*, 2025. 3
- [41] Manxi Lin, Nina Weng, Kamil Mikolaj, Zahra Bashir, Morten B. S. Svendsen, Martin G. Tolsgaard, Anders Ny-mark Christensen, and Aasa Feragen. Shortcut learning in medical image segmentation. In *Medical Image Computing and Computer Assisted Intervention – MICCAI 2024*, pages 623–633. Springer, 2024. 1
- [42] Wenye Lin and Kai Han. Surgical post-training: Cutting errors, keeping knowledge. *arXiv preprint arXiv:2603.01683*, 2026. 3
- [43] Wenye Lin, Jonathan Roberts, Yunhan Yang, Samuel Albanie, Zongqing Lu, and Kai Han. Gamebot: Transparent assessment of llm reasoning in games. In *Proceedings of the 63rd Annual Meeting of the Association for Computational Linguistics (Volume 1: Long Papers)*, pages 7656–7682, 2025. 2
- [44] Bo Liu, Li-Ming Zhan, Li Xu, Lin Ma, Yan Yang, and Xiao-Ming Wu. Slake: A semantically-labeled knowledge-enhanced dataset for medical visual question answering. In *2021 IEEE 18th International Symposium on Biomedical Imaging (ISBI)*, pages 1650–1654. IEEE, 2021. 5, 6, 9
- [45] Chuang Liu, Yichao Cao, Yingying Zhang, Xiu Su, and Haogang Zhu. Perturbating, tuning, and collaborating: Harnessing vision foundation models for single domain generalization on medical imaging. In *Proceedings of the AAAI Conference on Artificial Intelligence*, pages 5370–5378, 2025. 1
- [46] Dengcan Liu, Fengkai Yang, Xiaohan Wang, Shurui Yan, Jiajun Chai, Jiahao Li, Yikun Ban, Zhendong Mao, Wei Lin, and Guojun Yin. Cdrmm: Contrast-driven rubric generation for reliable and interpretable reward modeling. *arXiv preprint arXiv:2603.08035*, 2026. 3
- [47] Guangliang Liu, Haitao Mao, Bochuan Cao, Zhiyu Xue, Xitong Zhang, Rongrong Wang, Jiliang Tang, and Kristen Johnson. On the intrinsic self-correction capability of llms: Uncertainty and latent concept. *arXiv preprint arXiv:2406.02378*, 2024. 1, 2
- [48] Haotian Liu et al. Improved baselines with visual instruction tuning. *arXiv preprint arXiv:2310.03744*, 2024. 11
- [49] Jiayang Liu, Yuan Wang, Jiawei Du, Joey Tianyi Zhou, and Zuozhu Liu. Medcot: Medical chain of thought via hierarchical expert. In *Proceedings of the 2024 Confer-*

- ence on Empirical Methods in Natural Language Processing (EMNLP 2024), pages 17371–17389, 2024. 1, 3, 6
- [50] Weiting Liu, Han Wu, Yufei Kuang, Xiongwei Han, Tao Zhong, Jianfeng Feng, and Wenlian Lu. Automated optimization modeling via a localizable error-driven perspective. *arXiv preprint arXiv:2602.11164*, 2026. 3
- [51] Yajun Liu, Zenghui Zhang, Jiang Yue, and Weiwei Guo. Scanext: Enhancing 3d medical image segmentation with dual attention network and depth-wise convolution. *Heliyon*, 10(5), 2024. 3
- [52] Yajun Liu, Zenghui Zhang, Jiang Yue, Weiwei Guo, and Dongying Li. M 3 hl: Mutual mask mix with high-low level feature consistency for semi-supervised medical image segmentation. In *International Conference on Medical Image Computing and Computer-Assisted Intervention*, pages 314–323. Springer, 2025. 3
- [53] Ilya Loshchilov and Frank Hutter. Decoupled weight decay regularization. *arXiv preprint arXiv:1711.05101*, 2017. 6
- [54] Weijian Ma, Shizhao Sun, Tianyu Yu, Ruiyu Wang, Tat-Seng Chua, and Jiang Bian. Thinking with blueprints: Assisting vision-language models in spatial reasoning via structured object representation, 2026. 2
- [55] Aman Madaan, Niket Tandon, Prakhar Gupta, Skyler Hallinan, Luyu Gao, Sarah Wiegrefe, Uri Alon, Nouha Dziri, Shrimai Prabhumoye, Yiming Yang, Shashank Gupta, Bodhisattwa Prasad Majumder, Katherine Hermann, Sean Welleck, Amir Yazdanbakhsh, and Peter Clark. Self-refine: Iterative refinement with self-feedback. In *Advances in Neural Information Processing Systems*, pages 46534–46594, 2023. 2
- [56] Michael Moor, Qian Huang, Shirley Wu, Michihiro Yasunaga, Yash Dalmia, Jure Leskovec, Cyril Zakka, Eduardo Pontes Reis, and Pranav Rajpurkar. Med-flamingo: a multimodal medical few-shot learner. In *Machine Learning for Health (ML4H)*, pages 353–367. PMLR, 2023. 5, 6, 7
- [57] Viktor Moskvoretskii, Chris Biemann, and Irina Nikishina. Self-taught self-correction for small language models. *arXiv preprint arXiv:2503.08681*, 2025. 2
- [58] Long Ouyang, Jeffrey Wu, Xu Jiang, Diogo Almeida, Carroll Wainwright, Pamela Mishkin, Chong Zhang, Sandhini Agarwal, Katarina Slama, Alex Ray, et al. Training language models to follow instructions with human feedback. *Advances in neural information processing systems*, 35: 27730–27744, 2022. 3
- [59] Jiazhen Pan, Che Liu, Junde Wu, Fenglin Liu, Jiayuan Zhu, Hongwei Bran Li, Chen Chen, Cheng Ouyang, and Daniel Rueckert. Medvlm-r1: Incentivizing medical reasoning capability of vision-language models (vlms) via reinforcement learning. In *International Conference on Medical Image Computing and Computer-Assisted Intervention*, pages 337–347. Springer, 2025. 1, 2, 3, 5, 6, 11, 12
- [60] Yan Pan and Yuanzhi Li. Toward understanding why adam converges faster than sgd for transformers. *arXiv preprint arXiv:2306.00204*, 2023. 6
- [61] Lei Pang and Ruinan Jin. On the theory and practice of grpo: A trajectory-corrected approach with fast convergence. *arXiv preprint arXiv:2508.02833*, 2025. 3
- [62] Jonas Peters, Dominik Janzing, and Bernhard Scholkopf. *Elements of causal inference: foundations and learning algorithms*. MIT press, 2017. 2
- [63] Mattia Prosperi, Yi Guo, Matt Sperrin, James S Koopman, Jae S Min, Xing He, Shannan Rich, Mo Wang, Iain E Buchan, and Jiang Bian. Causal inference and counterfactual prediction in machine learning for actionable healthcare. *Nature Machine Intelligence*, 2(7):369–375, 2020. 2
- [64] Rafael Rafailov, Archit Sharma, Eric Mitchell, Christopher D Manning, Stefano Ermon, and Chelsea Finn. Direct preference optimization: Your language model is secretly a reward model. *Advances in neural information processing systems*, 36:53728–53741, 2023. 3, 9
- [65] Vishwanatha M Rao, Michael Hla, Michael Moor, Subathra Adithan, Stephen Kwak, Eric J Topol, and Pranav Rajpurkar. Multimodal generative ai for medical image interpretation. *Nature*, 639(8056):888–896, 2025. 1
- [66] Jonathan G Richens, Ciarán M Lee, and Saurabh Johri. Improving the accuracy of medical diagnosis with causal machine learning. *Nature communications*, 11(1):3923, 2020. 2
- [67] John Schulman, Filip Wolski, Prafulla Dhariwal, Alec Radford, and Oleg Klimov. Proximal policy optimization algorithms. *arXiv preprint arXiv:1707.06347*, 2017. 3
- [68] Zhihong Shao, Peiyi Wang, Qihao Zhu, Runxin Xu, Junxiao Song, Xiao Bi, Haowei Zhang, Mingchuan Zhang, YK Li, Yang Wu, et al. Deepseekmath: Pushing the limits of mathematical reasoning in open language models. *arXiv preprint arXiv:2402.03300*, 2024. 2, 3, 9
- [69] Noah Shinn, Federico Cassano, Ashwin Gopinath, Karthik Narasimhan, and Shunyu Yao. Reflexion: Language agents with verbal reinforcement learning. *Advances in Neural Information Processing Systems*, 36:8634–8652, 2023. 2
- [70] Haoming Song, Delin Qu, Yuanqi Yao, Qizhi Chen, Qi Lv, Yiwen Tang, Modi Shi, Guanghui Ren, Maoqing Yao, Bin Zhao, et al. Hume: Introducing system-2 thinking in visual-language-action model. *arXiv preprint arXiv:2505.21432*, 2025. 2
- [71] Yuqiao Tan, Minzheng Wang, Shizhu He, Huanxuan Liao, Chengfeng Zhao, Qiunan Lu, Tian Liang, Jun Zhao, and Kang Liu. Bottom-up policy optimization: Your language model policy secretly contains internal policies. *arXiv preprint arXiv:2512.19673*, 2025. 3
- [72] Ryutaro Tanno, David GT Barrett, Andrew Sellergren, Sumedh Ghaisas, Sumanth Dathathri, Abigail See, Johannes Welbl, Charles Lau, Tao Tu, Shekoofeh Azizi, et al. Collaboration between clinicians and vision-language models in radiology report generation. *Nature Medicine*, 31(2):599–608, 2025. 1
- [73] Athanasios Vlontzos, Christian Müller, and Bernhard Kainz. Causal reasoning in medical imaging. In *Trustworthy AI in Medical Imaging*, pages 367–381. Elsevier, 2025. 2
- [74] Lehan Wang, Haonan Wang, Honglong Yang, Jiaji Mao, Zehong Yang, Jun Shen, and Xiaomeng Li. Interpretable bilingual multimodal large language model for diverse biomedical tasks. *arXiv preprint arXiv:2410.18387*, 2024. 5, 6, 7, 11

- [75] Xuezhi Wang and Denny Zhou. Chain-of-thought reasoning without prompting. *arXiv preprint arXiv:2402.10200*, 2024. 2
- [76] Xuezhi Wang, Jason Wei, Dale Schuurmans, Quoc Le, Ed Chi, Sharan Narang, Aakanksha Chowdhery, and Denny Zhou. Self-consistency improves chain of thought reasoning in language models. *arXiv preprint arXiv:2203.11171*, 2022. 2
- [77] Yongxin Wang, Zhicheng Yang, Meng Cao, Mingfei Han, Haokun Lin, Yingying Zhu, Xiaojun Chang, and Xiaodan Liang. Care what fails: Contrastive anchored-reflection for verifiable multimodal. *arXiv preprint arXiv:2512.19554*, 2025. 3
- [78] Zehan Wang, Sashuai Zhou, Shaoxuan He, Haifeng Huang, Lihe Yang, Ziang Zhang, Xize Cheng, Shengpeng Ji, Tao Jin, Hengshuang Zhao, et al. Spatialclip: Learning 3d-aware image representations from spatially discriminative language. In *Proceedings of the Computer Vision and Pattern Recognition Conference*, pages 29656–29666, 2025. 2
- [79] Jason Wei, Xuezhi Wang, Dale Schuurmans, Maarten Bosma, Fei Xia, Ed Chi, Quoc V Le, Denny Zhou, et al. Chain-of-thought prompting elicits reasoning in large language models. *Advances in neural information processing systems*, 35:24824–24837, 2022. 2
- [80] Yanbin Wei, Qiushi Huang, Yu Zhang, and James Kwok. Kicgpt: Large language model with knowledge in context for knowledge graph completion. In *Findings of the association for computational linguistics: EMNLP 2023*, pages 8667–8683, 2023. 2
- [81] Yanbin Wei, Jianguye Yan, Chun Kang, Yang Chen, Hua Liu, James Kwok, and Yu Zhang. Dynamictr: Leveraging graph topology representation preferences to boost vlm capabilities on graph qas. *arXiv preprint arXiv:2602.21864*, 2026. 2
- [82] Chaoyi Wu, Xiaoman Zhang, Ya Zhang, Yanfeng Wang, and Weidi Xie. Towards generalist foundation model for radiology. *arXiv preprint arXiv:2308.02463*, 2023. 5, 6
- [83] Shuang Wu, Heng Liang, Yong Zhang, Yanlin Chen, and Ziyu Jia. A cross-modal densely guided knowledge distillation based on modality rebalancing strategy for enhanced unimodal emotion recognition. In *Proceedings of the Thirty-Fourth International Joint Conference on Artificial Intelligence, IJCAI 2025, Montreal, Canada, August 16–22, 2025*, pages 4236–4244, 2025. 2
- [84] Yuechen Xie, Jie Song, Huiqiong Wang, and Mingli Song. Training data provenance verification: Did your model use synthetic data from my generative model for training? In *Proceedings of the Computer Vision and Pattern Recognition Conference*, pages 23817–23827, 2025. 1
- [85] Yuechen Xie, Xiaoyan Zhang, Yicheng Shan, Hao Zhu, Rui Tang, Rong Wei, Mingli Song, Yuanyu Wan, and Jie Song. Spatialqa: A benchmark for evaluating spatial logical reasoning in vision-language models. *arXiv preprint arXiv:2602.20901*, 2026. 2
- [86] Zibo Xu, Qiang Li, Weizhi Nie, Weijie Wang, and Anan Liu. Structure causal models and llms integration in medical visual question answering. *IEEE Transactions on Medical Imaging*, 2025. 3
- [87] Fengkai Yang, Zherui Chen, Xiaohan Wang, Xiaodong Lu, Jiajun Chai, Guojun Yin, Wei Lin, Shuai Ma, Fuzhen Zhuang, Deqing Wang, et al. Your group-relative advantage is biased. *arXiv preprint arXiv:2601.08521*, 2026. 3
- [88] Shuo Yang, Caren Han, Yihao Ding, Shuhe Wang, and Eduard Hovy. Tooltree: Efficient llm tool planning via dual-feedback monte carlo tree search and bidirectional pruning. In *The Fourteenth International Conference on Learning Representations*. 3
- [89] Shuo Yang, Soyeon Caren Han, Xueqi Ma, Yan Li, Mohammad Reza Ghasemi Madani, and Eduard Hovy. Evotool: Self-evolving tool-use policy optimization in llm agents via blame-aware mutation and diversity-aware selection. *arXiv preprint arXiv:2603.04900*, 2026. 3
- [90] Ruilin Yao, Shengwu Xiong, Yichen Zhao, and Yi Rong. Visual grounding with multi-modal conditional adaptation. In *Proceedings of the 32nd ACM International Conference on Multimedia*, pages 3877–3886, 2024. 2
- [91] Jin Ye, Junlong Cheng, Jianpin Chen, Zhongying Deng, Tianbin Li, Haoyu Wang, Yanzhou Su, Ziyang Huang, Jilong Chen, Lei Jiang, et al. Sa-med2d-20m dataset: Segment anything in 2d medical imaging with 20 million masks. *arXiv preprint arXiv:2311.11969*, 2023. 5, 9
- [92] Shuang Zeng, Xinyuan Chang, Mengwei Xie, Xinran Liu, Yifan Bai, Zheng Pan, Mu Xu, and Xing Wei. Futuresight-drive: Thinking visually with spatio-temporal cot for autonomous driving. *arXiv preprint arXiv:2505.17685*, 2025. 3
- [93] Shuang Zeng, Dekang Qi, Xinyuan Chang, Feng Xiong, Shichao Xie, Xiaolong Wu, Shiyi Liang, Mu Xu, and Xing Wei. Janusvl: Decoupling semantics and spatiality with dual implicit memory for vision-language navigation. *arXiv preprint arXiv:2509.22548*, 2025. 3
- [94] Kai Zhang, Rong Zhou, Eashan Adhikarla, Zhiling Yan, Yixin Liu, Jun Yu, Zhengliang Liu, Xun Chen, Brian D Davison, Hui Ren, et al. A generalist vision-language foundation model for diverse biomedical tasks. *Nature Medicine*, 30(11):3129–3141, 2024. 5
- [95] Ruohong Zhang et al. Improve vision language model chain-of-thought reasoning. *arXiv preprint arXiv:2410.16198*, 2024. 2
- [96] Xiaoman Zhang, Chaoyi Wu, Ziheng Zhao, Weixiong Lin, Ya Zhang, Yanfeng Wang, and Weidi Xie. Pmc-vqa: Visual instruction tuning for medical visual question answering. *arXiv preprint arXiv:2305.10415*, 2023. 6
- [97] Sichen Zhao, Zhiming Xue, Yalun Qi, Xianling Zeng, and Zihan Yu. Non-intrusive graph-based bot detection for e-commerce using inductive graph neural networks. *arXiv preprint arXiv:2601.22579*, 2026. 2
- [98] Shuang Zhou, Mingquan Lin, Sirui Ding, Jiashuo Wang, Canyu Chen, Genevieve B Melton, James Zou, and Rui Zhang. Explainable differential diagnosis with dual-inference large language models. *npj Health Systems*, 2(1): 12, 2025. 4
- [99] Sashuai Zhou, Qiang Zhou, Jijin Hu, Hanqing Yang, Yue Cao, Junpeng Ma, Yinchao Ma, Jun Song, Tiezheng Ge, Cheng Yu, Bo Zheng, and Zhou Zhao. Unified thinker: A

general reasoning modular core for image generation, 2026. [2](#)

- [100] Yixiao Zhou, Ziyu Zhao, Dongzhou Cheng, Zhiliang Wu, Jie Gui, Yi Yang, Fei Wu, Yu Cheng, and Hehe Fan. Dropping experts, recombining neurons: Retraining-free pruning for sparse mixture-of-experts llms. In *Findings of the Association for Computational Linguistics: EMNLP 2025*, pages 15169–15186, 2025. [3](#)
- [101] Yixiao Zhou, Yang Li, Dongzhou Cheng, Hehe Fan, and Yu Cheng. Look inward to explore outward: Learning temperature policy from llm internal states via hierarchical rl. *arXiv preprint arXiv:2602.13035*, 2026. [3](#)
- [102] Daniel M Ziegler, Nisan Stiennon, Jeffrey Wu, Tom B Brown, Alec Radford, Dario Amodei, Paul Christiano, and Geoffrey Irving. Fine-tuning language models from human preferences. *arXiv preprint arXiv:1909.08593*, 2019. [3](#)